Journal of Hydrology 579 (2019) 124116

Contents lists available at ScienceDirect

Journal of Hydrology

journal homepage: www.elsevier.com/locate/jhydrol

Research papers

Hydrogeochemistry and geothermometry of the carbonate-evaporite aquifers controlled by deep-seated faults using major ions and environmental isotopes

Pingheng Yang[a,b,c,*], Dan Luo[a], Aihua Hong[c], Brian Ham[d], Shiyou Xie[a], Xiaoxing Ming[a], Zhixiang Wang[e], Zhonghe Pang[b,f,*]

[a] State Cultivation Base of Eco-agriculture for Southwest Mountainous Land, Field Scientific Observation & Research Base of Karst Eco-environments at Nanchuan in Chongqing, Ministry of Natural Resources, School of Geographical Sciences, Southwest University, Chongqing 400715, China
[b] Key Laboratory of Shale Gas and Geoengineering, Institute of Geology and Geophysics, Chinese Academy Sciences, Beijing 100029, China
[c] The Laboratory of Chongqing Groundwater Resource Utilization and Environmental Protection, Nanjiang Hydrogeological Team under the Chongqing Geological Bureau of Geology and Minerals Exploration, Chongqing 401121, China
[d] Tennessee Department of Environment and Conservation, Division of Water Resources, Nashville, TN 37243, USA
[e] 208 Hydrogeological Team under the Chongqing Geological Bureau of Geology and Minerals Exploration, Chongqing 400700, China
[f] University of Chinese Academy of Sciences, Beijing 100049, China

ARTICLE INFO

Keywords:
Thermal water
Carbonate rocks
Isotopes
Fault
Paleo-recharge
Southeast Chongqing in China

ABSTRACT

Carbonate aquifers probably constitute the most important thermal water resources in non-volcanic areas, and are characteristic of great energy potential and easier production as the most ideal targets for development in the future. The thermal waters in the aquifers within Southeast Chongqing (SEC) of China occur in an extensive region with an area of 198,000 km^2, which are mainly hosted in the Cambrian and Ordovician carbonate-evaporite rocks. The thermal waters are mainly in pristine conditions and their genesis has not yet been fully understood. The occurrence of thermal waters in SEC is closely related to the presence of deep-seated faults which constitute pathways for the hydrothermal circulation. In this study, an investigation of water major ions and environmental isotopes from 14 hot springs and three drilled wells was carried out to examine their hydrogeochemical evolution and to estimate reservoir temperature. The thermal waters have outflow temperatures from 19 to 54.2 °C. They are divided into two hydrochemical groups with the Yushan Fault as a boundary: Group A, located to the west of the fault, are characterized by facies of chloride sodium waters with higher TDS; Group B, to the east of the fault, are more complicated sulfate-bicarbonate-chloride alkaline-earth waters with lower TDS. The hydrochemical processes such as dissolution of carbonate, gypsum and/or anhydrite, and halite, the common ion effect, and dedolomitization are evident based on the major ions and $\delta^{34}S_{SO4}$ and $\delta^{18}O_{SO4}$. The $\delta^{18}O$ and δD compositions of the thermal waters suggest a meteoric recharge in a relatively wetter and colder climatic condition. The silica geothermometers show that the average reservoir temperatures are 63 ± 18 °C for Group A, and 82 ± 15 °C for Group B. The corresponding average reservoir depths are estimated to be 2.5 ± 0.7 km for Group A, and 3.2 ± 0.7 km for Group B. The corrected ^{14}C ages of the thermal waters average at 14.8 ka BP, corresponding to the late Pleistocene. A conceptual circulation model is proposed for the thermal waters. Driven by gravity of topographic gradients, the percolating groundwater circulates at a specific depth, reaching a higher temperature and interacting with the host carbonate with imbedded evaporitic minerals (gypsum and/or anhydrite, and additional halite for Group A) to be saline deep-seated thermal fluids. The fluids rise along faults and emerge at the surface as thermal springs. The slow renewability rate of the thermal aquifers highlights the importance of assessing the resource before groundwater exploitation and extraction.

* Corresponding authors at: 2 Tiansheng Road, Beibei District, Chongqing 400715, China (P. Yang). 19 Beituchengxi Road, Chaoyang District, Beijing 100029, China (Z. Pang).
E-mail addresses: balance@swu.edu.cn (P. Yang), z.pang@mail.iggcas.ac.cn (Z. Pang).

https://doi.org/10.1016/j.jhydrol.2019.124116
Received 12 May 2019; Received in revised form 11 August 2019; Accepted 4 September 2019
Available online 06 September 2019

1. Introduction

The occurrence of thermal water is associated with lithostratigraphic and structural conditions. The most intensively studied thermal water systems are those associated with active volcanic areas (e.g. Dobson et al., 2018; Kalacheva et al., 2018; Kavouridis et al., 1999; McMillan et al., 2018). However, carbonate aquifers probably constitute the most important thermal water resources outside of volcanic areas, which have received attention for their value in space heating, electric power generation, and recreational purposes (Goldscheider et al., 2010). Although there is no detailed and reliable global assessment of thermal water resources (Goldscheider et al., 2010), deep carbonate aquifers characterized by great energy potential and easier production are the most ideal targets for development (Kong et al., 2014; Pang et al., 2012, 2014). The thermal water resources in continental carbonate rock aquifers are normally related with deep and regional flow systems and characterized by trans-formational hydraulic continuity (e.g. Goldscheider et al., 2010; Tóth, 1995; Yang et al., 2013). Groundwater circulation in these situations can be described as a regional flow system which is generally gravity-driven by topographic gradients (Jiang et al., 2012; Mádl-Szőnyi and Tóth, 2015; Tóth, 1963; Yang et al., 2017). The precipitation falling in the higher-elevation regions percolates into the aquifer, and is heated to result in deep-seated thermal fluids. Ascending thermal fluid paths are generally controlled by faults and fracture zones. which represent zones of enhanced permeability (Qiu et al., 2018; Stober et al., 2016).

However, most of the carbonate thermal waters at great depths with deep water circulation are often poorly understood (Goldscheider et al., 2010). Geochemistry and isotopes are indispensable tools for studying the hydrogeologic structure and functioning of these systems. Geochemical and isotopic techniques applied during stages of exploration and evaluation of geothermal resources, as well as monitoring studies, are particularly important because of the information they provide relatively fast and at low cost (D'Amore and Arnórsson, 2000a; Fournier, 1977). Moreover, thermal waters including springs and well water potentially provide information on geochemical processes acting deep within aquifers (Gunn et al., 2006). As such, investigation of the geochemical and related isotopic characteristics of thermal waters is always one of first steps in the evaluation of the geothermal potential of an area. The basic approaches of studying thermal waters are to use the major ions, stable isotopes and radioisotope data to define hydrochemical characteristics, the source of major ions and water, groundwater residence time and other hydrodynamic features (e.g. Aquilina et al., 2003; Gunn et al., 2006; Ma et al., 2011; Utting et al., 2013; Yang et al., 2017). The application of geochemical and isotopic methods in thermal exploration thus can provide very useful information on geochemical evolution, water circulation, and water-rock interactions within the carbonate aquifers that are difficult to obtain by other techniques.

Moreover, a crucial point in the exploration of thermal water resources is to know the precise temperature at depth of a particular geothermal reservoir. The most reliable temperatures are obtained by static bottom-hole temperature surveys for exploratory or production wells. However, this way of temperature surveying, although often inevitable, is the most expensive approach due to the costly investment for exploratory drilling (Adam and Jan, 2009). The application of chemical and isotopic groundwater temperature indicators, the so-called geothermometers, is based on temperature-dependent water–-rock chemical equilibrium (chemical reactions or isotope equilibrium fractionation relations) from which the equilibrium temperatures can be estimated (D'Amore and Arnórsson, 2000b). The geothermometrical methods mainly include cation geothermometers (e.g. Fournier and Truesdell, 1973; Giggenbach, 1988; Verma and Santoyo, 1997), silica geothermometers (e.g. Fournier, 1977; Verma and Santoyo, 1997), isotopic geothermometers (e.g. Blasco et al., 2018; Lloyd, 1968), and the theoretical geothermometer based on chemical thermodynamic modelling (e.g. Pang and Reed, 1998). The estimated temperatures for the deep reservoir allow reducing the cost of geothermal exploration.

In China, geothermal resources of the major basins are $24{,}964.4 \times 10^{18}$ J, which is equivalent to 8531.9×10^{8} tons of standard coal. The geothermal resources within the Sichuan basin account for the largest portion, calculated to be as much as 31% of the total geothermal resources in China (Wang et al., 2013). Located in east Sichuan basin, Chongqing Municipality has 107 areas that include thermal water resources, and some of them are stored in Triassic carbonate rock aquifers within the urban area (e.g. Ta et al, 2019; Xiao et al., 2018; Yang et al., 2017, 2019). The hydrogeochemistry of the carbonate thermal water within the urban area of Chongqing were investigated in detail, showing that high concentrations of Ca^{2+} and SO_4^{2-} in the thermal waters are derived from the dissolution of gypsum and/or anhydrite (Xiao et al., 2018; Yang et al., 2017, 2019), and reservoir temperatures were estimated to be 64.8–93.4 °C, averaging at 82 °C (Yang et al., 2017). However, compared to the urban area, the hydrogeochemistry and geothermometry of the carbonate thermal waters within southeastern Chongqing (SEC) are still unknown and no literature about the hydrothermal characteristics is available, which is probably attributable to the remote location and complex geology of the area. Moreover, the social and economic development value will be elevated as the construction for the high-speed rail connecting the urban area and the SEC (Fig. 1a) will be completed in 2024. The demand for thermal water resources will inevitably be increasing within SEC, which requires a thorough investigation of the hydrothermal aquifers for their potential and renewability for exploitation. This task is impossible to achieve without knowledge of the hydrogeochemistry and geothermometry within SEC. It is therefore highly necessary to bridge the gap of knowledge for the thermal aquifers within SEC. The study mainly aims to (1) characterize the hydrochemical properties of the thermal waters, (2) understand the water-rock interaction processes occurring at depth, (3) determine the recharge times, and estimate the geothermal reservoir temperatures and their corresponding depths, and (4) propose a conceptual hydrogeological model for genesis of the thermal waters. To achieve these objectives, a combination of methods including geochemistry (major ions), isotopes ($^{34}S_{SO4}$, $^{18}O_{SO4}$, $^{18}O_{H2O}$, $^{2}H_{H2O}$, $^{13}C_{DIC}$, $^{14}C_{DIC}$), and geothermometers were used to study the hydrothermal systems.

The methodological approaches utilized in this study are more relevant and useful in similar geological, hydrogeological, and geochemical frameworks characterized by fault-controlled, low-temperature carbonate hydrothermal systems.

2. Study area

2.1. Geographical settings

Geographically, the SEC is located in the southeast part of Chongqing Municipality (Fig. 1a). It includes the Districts of Qianjiang and Wulong, Counties of Shizhu, Youyang, Pengshui, and Xiushan. The local mean annual air temperature and rainfall are approximately 16.6 °C and 1300 mm, respectively. The landscape is dominated by hilly terraces with a relative elevation difference of 500–1000 m. Functioning as the local base level of erosion, several rivers run through the study area, such as Wu River, Zhufo River, and A'peng River. In this study, for chemical and isotopic analysis, a total of 14 hot spring sites and three geothermal drilled wells from SEC were obtained during December 2017 and June 2018. All of the sample points and their sampling nos. are shown in Fig. 1a. The original set of chemical and isotopic data of thermal fluids discharge from a region with an area of 19,800 km^2 which accounts for approximately 20% of Chongqing municipality, comprised between N 28°–30° and E 107.5°–109.3°, as shown in Fig. 1a.

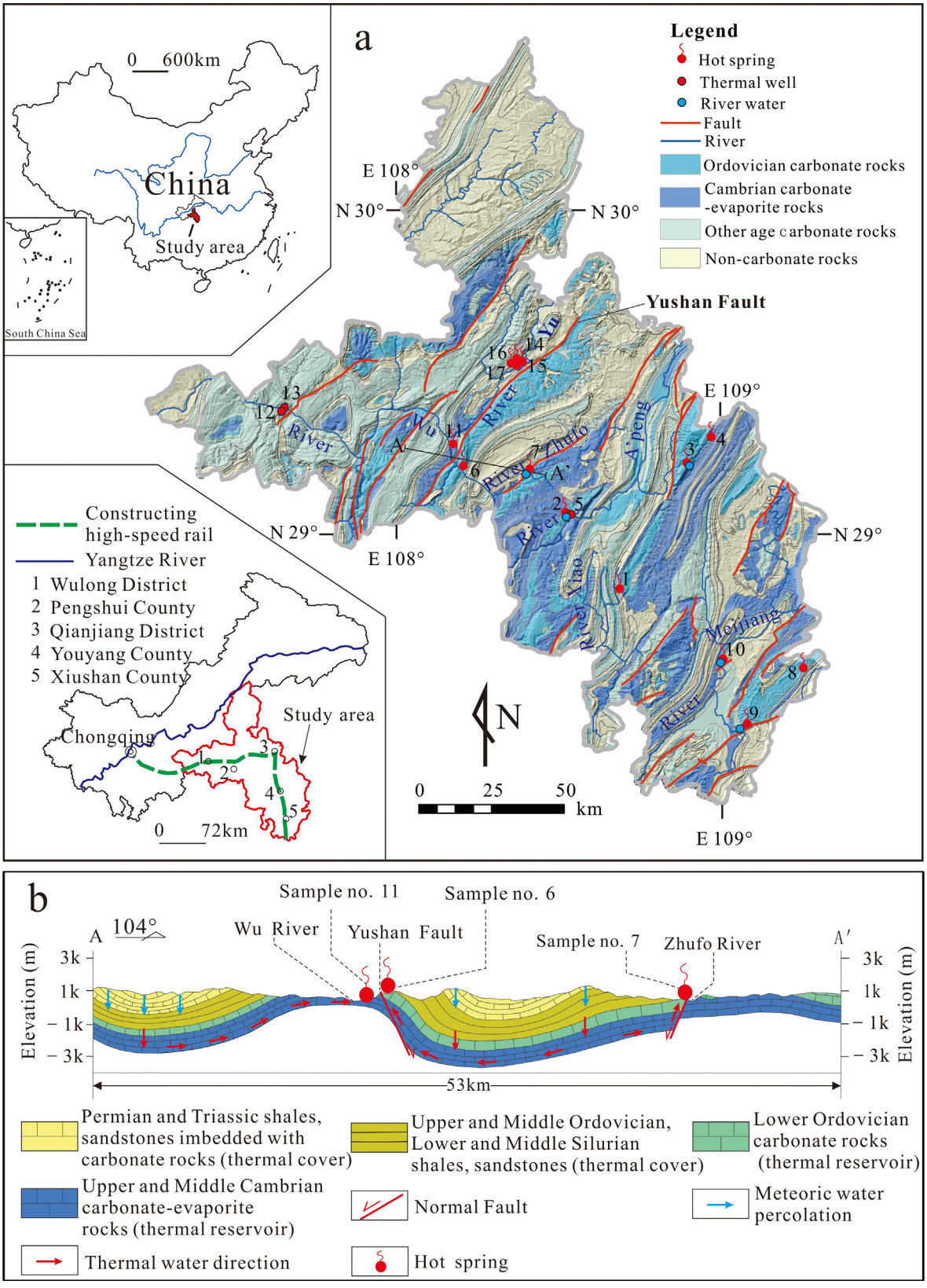

Fig. 1. (a) Generalized geology and location of the thermal waters within SEC; (b) Schematic hydrogeological and structural cross-sections of A–A′ reported in (a). The study area is characterized by a series of parallel anticlines and synclines trending NE–SW. Most of the thermal waters align along the faults and rivers.

2.2. Geological and hydrogeological settings

The SEC is characterized by a series of parallel and trending NE–SW folds with alternating anticlines and synclines (Fig. 1b). Stratigraphically, the outcropping formations include Paleozoic to Quaternary sedimentary layers, lacking the Upper Silurian, Devonian, Carboniferous formations due to paleo erosion. The Lower Cambrian stratum consists of siltstone and shale with a thickness of > 373 m

(GBSP, 1979). The Upper and Middle Cambrian strata are limestone and dolomitic limestone with a thickness of 1044–1322 m, which are imbedded with evaporites (halite, gypsum and/or anhydrite), indicating the transition to a paralic continental environment. The Lower Ordovician formations are composed of limestone, dolomite and bioclastic limestone with a thickness of 228–294 m. The Middle and Upper Ordovician, Middle and Lower Silurian strata mainly consist of shale and sandstone, up to 2000 m thick. The Permian and Triassic strata are composed of shale, marl, and limestone containing chert nodules, with a thickness of 1190–2009 m. The Jurassic and Cenozoic formations are composed of shale, sandstone, and breccia, which were uplifted and partially eroded. The Quaternary formation is distributed sporadically. Faults are well-developed with the NE–SW trend and dip to the northwest at around 60° in the study area. Most faults are developed in limbs of the anticlines and cut through the Ordovician and Cambrian carbonate formations at depths more than 3 km (Fig. 1b).

Accounting for almost 55% of the study area, the carbonate aquifers mainly consist of limestone and dolomite with resurgences via hot and shallow karst springs with an average runoff of 4.5 L/s per km^2. The hydrothermal systems within SEC are manifested by hot springs emerging around the faults at elevations of 184–960 m a.s.L.. These hot springs are artesian and issue from Cambrian and Ordovician carbonate rocks mainly aligned along the faults (Fig. 1a). The deep-seated faults are assumed to be major controls on groundwater flow, and act as preferential pathways for thermal water ascent. Stratigraphically, the hot springs are located at the flanks of anticlines. In the context of this study, the Upper and Middle Cambrian and the Lower Ordovician carbonate-evaporite rocks are of special interest in the study area as they constitute the potential geothermal reservoir for the thermal springs. These geothermal formations are affected by a highly developed deep-seated fault system which could be responsible for the regional hydrothermal activities, especially where permeability is enhanced by well-developed faulting, fracturing, and karstification processes. The geothermal reservoir is highly permeable with a hydraulic conductivity of 11.5 m/d calculated by the pumping test from the aquifer around sample no. 12. The thermal cover layer consists of the Middle and Upper Ordovician, Silurian, Permian, and Triassic strata more than 3000 m thick. The Lower Cambrian stratum below the carbonate-evaporite rocks serves as the semi-confining bed underlying the thermal reservoir. The regional terrestrial heat flow and average geothermal gradient are about 53.7 ± 8.7 mW/m^2 (Jiang et al., 2019) and 21 °C/km with depth (see Section 5.3), respectively. The hydrogeochemistry and possible sulfate sources of the shallow karst groundwaters in the study area were investigated by Pu et al. (2013).

Most hot springs are not used, and discharge into the rivers, except samples nos. 9 and 10 which are used for spa and therapeutic purposes by the local residents. In recent years, three geothermal wells (samples nos. 3, 12 and 13) were drilled and provide thermal water for the commercial spa.

3. Methodology and materials

3.1. Sampling and measurements

Water temperature, pH, and specific conductivity (spC) were directly measured in the field using a WTW Multi3630 probe (WTW, Germany), with accuracies of 0.1 °C, 0.01pH unit, and 1μS/cm, respectively. The HCO_3^- concentration was determined in the field by titration with an alkalinity kit (Merck, Germany), with an accuracy of 0.61 mg/L.

Prior to sampling, the water was filtered with φ0.45 μm membrane filters and injected into 15, 500, 500, and 4500 mL high-density polyethylene bottles, respectively for measuring δD and $\delta^{18}O$, cations, anions, and sulfur and oxygen isotope compositions of dissolved sulfate ($\delta^{34}S_{SO4}$ and $\delta^{18}O_{SO4}$). The water samples for analyzing radiocarbon activity concentrations ($A^{14}C_{DIC}$) and stable carbon isotope composition of dissolved inorganic carbon ($\delta^{13}C_{DIC}$) were promptly sampled in a 1 L high-density polyethylene bottle to avoid mixing with air CO_2. Before collecting thermal water samples, all sampling bottles were flushed with the same thermal water which was to be sampled later. The samples for cation measurement were acidified by adding nitric acid to make the pH < 2 immediately after sampling. All sample bottles were carefully sealed with airtight caps and were refrigerated at 4 °C to minimize bacterial growth.

Major cations were determined by 5110 inductively coupled plasma-optical emissions spectroscopy (ICP-OES, Perkin Elmer, USA) with an accuracy of 0.01 mg/L. Major anions were measured by a T6 ultraviolet and visible spectrophotometer (Persee, China) with an accuracy of 0.01 mg/L. The above major ions were measured at Geotechnical Engineering Testing Center of Chongqing, China. A total of nine thermal water samples (nos. 1–4, 7, 8, 10, 16, and 17) were analyzed for $\delta^{34}S_{SO4}$, and seven samples (nos. 1–4, 7, 8, and 10) were measured for $\delta^{18}O_{SO4}$. Before measurement, the thermal water samples were acidified to pH < 4 to remove bicarbonate. Then the water samples were precipitated as $BaSO_4$. The precipitate was recovered by filtration, carefully washed with distilled water, and dried prior to isotope analyses. The $\delta^{34}S_{SO4}$ values are reported relative to the Vienna Canyon Diablo Troilite standard (VCDT), and the $\delta^{18}O_{SO4}$ values are relative to Vienna Standard Mean Ocean Water (VSMOW). The mean standard deviations were 0.2‰ for $\delta^{34}S_{SO4}$ and 0.3‰ for $\delta^{18}O_{SO4}$, respectively. The $\delta^{34}S_{SO4}$ and $\delta^{18}O_{SO4}$ values were measured with a DELTA V Plus isotope-ratio mass spectrometer (IRMS) at the State Key Laboratory of Biogeology and Environmental Geology in Wuhan, China. The $A^{14}C_{DIC}$, $\delta^{13}C_{DIC}$, and δD and $\delta^{18}O$ of five thermal water samples (nos. 1, 2, 7, 10, and 16) were measured at Beta Analytic Inc. (Miami, Florid, USA). The $A^{14}C_{DIC}$ concentrations were determined by accelerator mass spectrometry (NEC, US) with 1σ. The $A^{14}C_{DIC}$ contents are reported in pMC (percent Modern Carbon). The $\delta^{13}C_{DIC}$, δD and $\delta^{18}O$ were measured by Delta-Plus IRMS (Thermo Fisher Scientific, US) with accuracies of 0.3‰, 2‰ and 0.3‰, respectively. While the $\delta^{13}C_{DIC}$ of samples nos. 3, 4, 6, 8, 9, 13, and 17 were determined by MAT253 (Finnigan, Germany) with accuracies of 0.15‰ in the Institute of Karst Geology, Chinese Academy of Geological Sciences, Guilin, China, their corresponding δD and $\delta^{18}O$ values were measured by a Liquid Water Isotope Analyzer (Los Gatos Research Inc., USA), with mean standard deviations of 0.3‰, 0.1‰ for δD and $\delta^{18}O$, respectively, which were carried out in the Geochemistry and Isotope Laboratory, School of Geographical Sciences, Southwest University, Chongqing, China. The $\delta^{13}C_{DIC}$ values are relative to Vienna Pee Dee Belemnite (VPDB). The δD and $\delta^{18}O$ values are reported relative to VSMOW.

All major ion concentrations and isotopic data relative to the 17 thermal waters from SEC are reported in Table 1. The ionic charge imbalance between the sum of major cations and anions, and saturation indices (SIs) for the thermal water samples were calculated with a geochemical PHREEQC code (Parkhurst and Appelo, 2013). The results showed that all the samples have an ionic charge imbalance of ≤ ± 5%.

3.2. Geothermometers

The application of geothermometers is based on several assumptions: that chemical equilibrium is established between the waters and rock; there is an adequate supply of chemical reactants; and there is no chemical re-equilibrium during ascent of the hot water (Fournier, 1977; Fournier and Truesdell, 1974). The sulfate-water $\delta^{18}O$ pair ($\delta^{18}O_{SO4\text{-}H2O}$) geothermometer is based on the assumption that two species are in isotopic equilibrium with respect to oxygen and the isotope exchange is a function of temperature (Lloyd, 1968), which was widely used in some thermal aquifers (e.g. Adam and Jan, 2009; Awaleh et al., 2015; Pang, 2001). The silica geothermometers, cation geothermometers, and $\delta^{18}O_{SO4\text{-}H2O}$ geothermometer were employed in this study. Their equations were expressed as follows:

Table 1
Major ions concentrations and isotopic data of the thermal waters within SEC. The water temperature (T) is in ˚C; the major element concentrations and TDS are in mg/L; δD, $\delta^{18}O$ and $\delta^{18}O_{SO4}$ are in ‰ (VSMOW); $\delta^{34}S_{SO4}$ is in ‰ (VCDT); $\delta^{13}C_{DIC}$ is in ‰ (VPDB); $A^{14}C_{DIC}$ is in pMC; Uncorrected and corrected ages are in a (yr); – denotes species that were not analyzed.

Sampling ID	T	pH	K^+	Na^+	Ca^{2+}	Mg^{2+}	HCO_3^-	Cl^-	SO_4^{2-}	NO_3^-	SiO_2	TDS	δD	$\delta^{18}O$	$\delta^{34}S_{SO4}$	$\delta^{18}O_{SO4}$	$\delta^{13}C_{DIC}$	$A^{14}C_{DIC}$	Uncorrected age	Corrected age
1	29.6	7.12	8.10	2.13	500	114	130	1.76	1520	0.64	31.7	2364	−63.3	−9.7	32.0	15.3	−5.90	4.4	25,020	21,171
2	27.8	7.26	18.7	181	196	34.2	174	295	466	0.64	66.2	1,511	−61.7	−9.2	33.6	13.7	−6.30	15.9	14,780	10,310
3	37.7	7.63	0.68	0.14	57.8	21.8	152	4.39	87.6	0.91	16.8	363	−65.0	−9.7	25.3	9.2	−6.63	–	–	–
4	30.5	7.36	8.60	4.95	498	98.9	125	3.38	1511	0.64	33.4	2341	−64.3	−9.5	32.4	16.2	−5.57	–	–	–
5	54.2	7.62	3.60	3.66	62.4	16.8	166	4.30	93.7	1.43	29.8	414	–	–	–	–		–	–	–
6	42.0	8.00	6.35	6.61	124	48.0	198	5.52	328	0.73	27.8	781	−62.0	−9.1	–	–	−8.63	–	–	–
7	34.1	7.21	6.13	9.14	171	41.8	116	9.54	512	3.96	30.8	848	−61.0	−9.2	37.4	13.2	−6.40	5.7	23,070	18,833
8	48.3	6.81	9.58	2.70	277	43.4	170	4.53	698	0.62	42.6	1307	−56.0	−8.5	31.2	15.0	−6.02	–	–	–
9	34.1	7.20	0.94	0.62	59.2	24.3	247	0.44	56.1	0.64	23.9	449	−50.0	−7.9	18.5	6.8	−9.27	–	–	–
10	45.5	6.86	2.11	4.71	99.9	2.5	226	2.97	83.2	5.12	30.7	504	−52.7	−8.3	29.3	13.2	−9.70	20.4	12,760	8998
11	53.0	7.11	66.5	2250	466	3.0	173	3477	1130	0.28	38.2	766	–	–	–	–		–	–	–
12	43.0	7.05	68.8	3406	625	134	120	5590	1627	0.34	26.4	11,611	–	–	–	–	−9.01	–	–	–
13	43.0	7.02	68.5	3374	617	127	129	5626	1669	0.38	26.0	11,683	−62.1	−9.2	–	–		–	–	–
14	23.0	7.22	172	8160	680	128	179	12,617	1953	0.23	21.7	23,756	–	–	–	–	–	–	–	–
15	19.0	7.39	105	5194	458	20.2	210	8018	936	0.89	15.4	14,989	–	–	–	–	–	–	–	–
16	27.2	7.99	18.8	842	178	30.3	201	1343	187	6.48	9.3	2637	−41.8	−7.0	29.6	–	−13.10	83.9	1410	−4099 (modern)
17	22.3	7.21	74.4	2826	70.8	201	220	4610	646	4.08	13.1	8691	–		32.1	–	−10.96		–	–

(1) Quartz (Fournier, 1977), $t_{SiO2} = [1309/(5.19 - lgS)] - 273.15$
(2) Improved SiO_2 (Verma and Santoyo, 1997), $t_{SiO2} = -44.119 + 0.24469S - 1.7414 \times 10^{-4}S^2 + 79.305lgS$
(3) K-Mg (Giggenbach, 1988), $t_{K\text{-}Mg} = 4410/[(14.0 - lg(K^2/Mg)] - 273.15$
(4) Na-K (Giggenbach, 1988), $t_{Na\text{-}K} = 1390/[1.75 - lg(Na/K)] - 273.15$
(5) Na-K-Ca (Fournier and Truesdell, 1973), $t_{Na\text{-}K\text{-}Ca} = 1647/[lg(Na/K) + (4/3)lg(\sqrt{Ca}/Na) + 2.24] - 273.15$
(6) The pair sulfate-water $\delta^{18}O_{SO4}$ and $\delta^{18}O_{H2O}$ (Lloyd, 1968), $ln\alpha = 3251/T^2 - 0.0056$

where, *t* is the estimated reservoir temperature in ˚C; *T* is the estimated reservoir temperature in Kelvin degree; *S* is the SiO_2 concentration in mg/L; K, Mg, Na, and Ca are their corresponding concentrations in mg/L; *α* is the fractionation factor between $^{18}O_{SO4}$ and $^{18}O_{H2O}$.

4. Results

4.1. Hydrochemistry

The thermal waters have discharging temperatures from 19 to 54.2 ˚C (Table 1), with an average of 36.1 ± 10.8 ˚C, which is significantly higher than the average annual local air temperature of 16.6 ˚C and belongs to low-temperature thermal water. The different outlet temperatures of the thermal springs are probably ascribed to local conditions depending on the velocity of water flow and time of residence. Values of pH range between 6.8 and 8 (Table 1), averaging at 7.3 ± 0.3, which shows a neutral to weak alkaline aquifer condition.

A Piper triangular diagram is a useful method for plotting the results of multiple analyses in the same graph, which can reveal grouping of certain samples and show different hydrochemical characteristics (Piper, 1944). A Schoeller diagram (Fig. 2b) illustrates how the main variations appear precisely in these ions, in which two different categories of the thermal waters can also be recognized. On the basis of the Piper plot (Fig. 2a) and Schoeller diagram (Fig. 2b), and the TDS values (Fig. 2a, Table 1), the thermal waters of the study area are classified into two hydrochemical categories, which showed strong variations in the space divided by the Yushan Fault: Group A (nos. 11–17) within the west of Yushan Fault is characterized by facies of chloride sodium waters with higher TDS, ranging from 766 to 23,956 mg/L and averaging at 10,619 ± 7784 mg/L, while Group B (nos. 1–10) within the east of Yushan Fault is dominated by complex geochemical facies with sulfate-bicarbonate-chloride alkaline-earth waters with relatively lower TDS, ranging between 363 and 2364 mg/L and averaging at 1088 ± 768 mg/L. Specifically, the chemical compositions of Group B are highly variable, including SO_4–Ca·Mg (nos. 1, 4, 7 and 8), HCO_3·SO_4–Ca·Mg (nos. 3, 5, 6, 9), HCO_3·SO_4–Ca (no. 10), and SO_4·Cl–Ca·Na (no. 2). Hydrogeologically, the two totally different facies confirm the influence of the geological formations dominated by Cambrian carbonate-evaporite rocks, and separate groundwater flow systems.

The mineral composition of the thermal waters reflects the geological formations (Chenaker et al., 2018). For cations, the Ca^{2+} concentrations are in the range of 70.7 to 680 mg/L, averaging at 442 ± 234 mg/L for Group A, and 57.8 to 500 mg/L, averaging at 204.6 ± 170 mg/L for Group B. The Mg^{2+} concentrations range from 3.0 to 201 mg/L, averaging at 92 ± 74.3 mg/L for Group A, and 2.5 to 114 mg/L, averaging at 44.6 ± 35.6 mg/L for Group B. The Na^+ concentrations vary from 842 to 8160 mg/L, averaging at 3722 ± 2357 mg/L for Group A, and from 0.14 to 180.9 mg/L averaging at 21.6 ± 56.1 mg/L for Group B. The K^+ concentrations range from 18.8 to 171.9 mg/L, averaging at 82 ± 47 mg/L for Group A, and from 0.68 to 18.7 mg/L, averaging at 6.5 ± 5.4 mg/L for Group B. The mean concentrations of the major cations for Group A are much higher

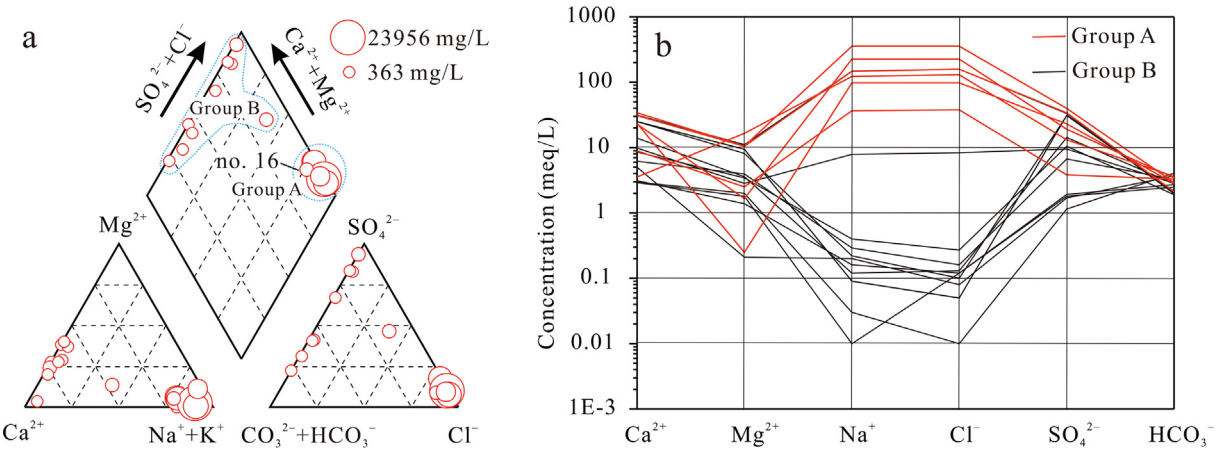

Fig. 2. (a) Piper plot and (b) Schoeller diagram of the thermal waters. The diagrams show that the thermal waters can be classified into two distinct categories: Group A has facies of chloride sodium waters with higher TDS values; Group B is characterized by complex geochemical facies with bicarbonate-sulfate-chloride alkaline-earth waters and relatively lower TDS values.

than those of Group B. All the major cation concentrations of the thermal waters are significantly higher than those of the shallow karst groundwaters of the study area (n = 11) from Pu et al. (2013), which reported average concentrations of 54.2 mg/L for Ca^{2+}, 13.8 mg/L for Mg^{2+}, 1.7 mg/L for Na^{+}, and 1.3 mg/L for K^{+}.

For anions, the Cl^{-} concentrations vary from 1343 to 12,617 mg/L, with an average of 5897 ± 3607 mg/L for Group A, and from 0.44 to 295 mg/L, averaging at 33.2 ± 91.9 mg/L for Group B. The halite dissolution causes the significantly higher Cl^{-} and Na^{+} concentrations of Group A (see Section 5.1). The SO_4^{2-} concentrations range from 187 to 1953 mg/L, with a mean value of 1164 ± 628 mg/L, and from 56.1 to 1520 mg/L, averaging at 536 ± 560 mg/L for Group B. The SO_4^{2-} concentrations in the thermal waters are remarkably higher than those of the shallow karst groundwaters of the study area measured at a mean of 19.6 mg/L by Pu et al. (2013). This is in agreement with the high sulfate concentrations that frequently occur in thermal springs that discharge from carbonate aquifers (Blasco et al., 2017; Bouchaou et al., 2017; Goldscheider et al., 2010; Yang et al., 2017). The HCO_3^{-} concentrations vary between 120 and 220 mg/L, averaging at 176 ± 39 mg/L for Group A, and between 116 and 247 mg/L, averaging at 170 ± 43 mg/L for Group B, which is similar with those of the shallow karst groundwaters of the study area measured at 183 mg/L averagely by Pu et al. (2013). The average NO_3^{-} concentrations are 1.8 ± 2.5 mg/L for Group A, and 1.5 ± 1.6 mg/L for Group B, which is remarkably lower than those of the shallow karst groundwaters measured at 12.7 mg/L in average by Pu et al. (2013), indicating that the thermal aquifers are "isolated" from anthropogenic contamination.

According the classification of water based on TDS (Carpenter, 1977), the TDS values show that most thermal waters in Group A can be classified into brackish or saline water, except sample no. 11 which indicates fresh water with a TDS value of 766 mg/L. Among Group B, samples nos. 1, 2, 4 and 8 are brackish, while others are characterized as fresh water. Generally, Cl^{-} and Na^{+} are the major constituents that generate the overall salinity, followed by SO_4^{2-}, Ca^{2+}, and Mg^{2+} in Group A, while SO_4^{2-}, Ca^{2+}, Mg^{2+}, and HCO_3^{-} are the main constitutes generating the brackish condition in Group B. The chemical and physical properties of water depend on the amount and compositions of dissolved materials, the migration depth, the residence time of the water in the migration pathway, and rock-water interactions in formations (Chenaker et al., 2018). Most major element concentrations and TDS in the thermal waters are remarkably higher than those of shallow karst groundwaters (Pu et al., 2013), suggesting that existence of totally different hydrogeological environments between the thermal waters and the shallow karst groundwater. Generally, the occurrence of these thermal waters, as well as their chemical characteristics, seem to indicate the existence of large-scale/regional deep-seated groundwater flow systems, while the shallow karst groundwaters represent the local flow systems (Tóth, 1963).

Table 2
Saturation indices of the thermal waters within SEC.

Sampling ID	SIa (Anhydrite)	SIc (Calcite)	SId (Dolomite)	SIg (Gypsum)	SIh (Halite)	SIq (Quartz)
1	−0.3	0.0	−0.3	−0.1	−10.1	0.8
2	−1.0	0.1	−0.4	−0.8	−5.9	1.1
3	−2.0	0.0	−0.1	−1.7	−10.8	0.5
4	−0.3	0.3	0.1	−0.1	−9.4	0.8
5	−1.9	0.1	−0.1	−1.7	−9.4	0.7
6	−1.3	0.7	1.3	−1.0	−9.0	0.7
7	−1.0	−0.2	−0.8	−0.7	−8.7	0.8
8	−0.7	−0.3	−1.1	−0.5	−9.5	0.9
9	−2.2	−0.2	−0.5	−1.9	−11.1	0.7
10	−1.8	−0.4	−2.1	−1.5	−9.4	0.8
11	−0.7	0.0	−1.8	−0.4	−3.8	0.9
12	−0.5	−0.1	−0.6	−0.3	−3.5	0.7
13	−0.5	−0.1	−0.7	−0.3	−3.5	0.7
14	−0.6	0.2	−0.1	−0.4	−2.8	0.7
15	−0.9	0.3	−0.4	−0.7	−3.1	0.5
16	−1.5	0.8	1.0	−1.3	−4.6	0.2
17	−1.7	−0.6	−0.4	−1.5	−3.6	0.4

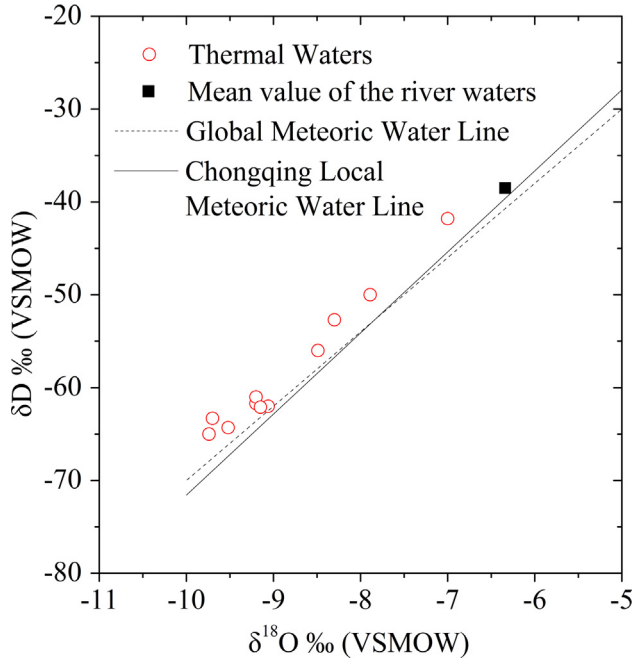

Fig. 3. δD vs. $\delta^{18}O$ of the thermal waters within SEC. The thermal waters distribute near the Global Meteoric Water Line (Craig, 1961) and Chongqing Local Meteoric Water Line (Li et al., 2010), suggesting that the thermal waters originate from local meteoric water. The depleted ^{18}O and ^{2}H isotopes comparison with local river waters suggests that the thermal waters are recharged at a relatively cooler and wetter climate condition.

4.2. Saturation indices

The calculated thermodynamic equilibrium SIs of the thermal waters are presented in Table 2. The SIs of anhydrite, gypsum and halite of the samples are undersaturated, indicating that these minerals are anticipated to dissolve. SIs of calcite and dolomite are negative and positive, showing that the solution varies between oversaturation and undersaturation. Samples are almost oversaturated with respect to quartz.

4.3. Isotopic compositions

The $\delta^{18}O$ values range from −9.2 to −7.0‰ (a mean value of −8.1‰) for Group A (n = 2), and from −9.7 to −7.9‰ (a mean value of −9.0 ± 0.6‰) for Group B (n = 9). The δD values vary between −62.1 and −41.8‰ with an average of −52.0‰ for Group A (n = 2), and between −65.0 and −50.0‰ with an average of −59.5 ± 5.4‰ for Group B (n = 9). All of the thermal waters are situated along the Global Meteoric Water Line (GMWL) defined by Craig (1961) and the Chongqing Local Meteoric Water Line (CLMWL: $\delta D = 8.3\ \delta^{18}O + 15.46$) carried out by Li et al. (2010) (Fig. 3) without indications of evaporation or water-rock interactions (i.e., enrichment of ^{18}O). This suggests that the thermal waters originate from local meteoric water.

The $\delta^{34}S_{SO4}$ values are from 29.6 to 32.1‰, with an average of 30.9‰ for Group A (n = 2), and from 25.3 to 37.4‰, with an average of 31.6 ± 3.7‰ for Group B (n = 7) (Table 1). The average $\delta^{34}S_{SO4}$ values of both Group A and Group B are significantly higher than those of shallow karst groundwaters reported at a mean of 6.6‰ by Pu et al. (2013). None of the thermal waters of Group A were measured for $\delta^{18}O_{SO4}$, while the $\delta^{18}O_{SO4}$ values range from 9. 2 to 16.2‰ averaging at 13.7 ± 2.3‰ for Group B (n = 7).

In Group A, the $\delta^{13}C_{DIC}$ values are in the range of −13.1 to −9‰, with an average of −11 ± 2‰ (n = 3). For Group B, the $\delta^{13}C_{DIC}$ data are in the range between −9.7 and −5.6‰, with an average of −7.2 ± 1.6‰ (n = 9). The $A^{14}C_{DIC}$ concentrations of sample no.16 sample is 83.9 pMC in Group A, and values range from 4.4 to 20.4 pMC with an average of 11.6 ± 7.8 pMC for Group B (n = 4) (Table 1). The uncorrected ages of the thermal water range from 13 to 25 ka BP, except for sample no. 16 with a value of 1.4 ka BP (Table 1). Except for sample no. 16, thermal waters (n = 4) are characterized by low $A^{14}C_{DIC}$ and high $\delta^{13}C_{DIC}$ values, suggesting a deep-seated fluid flow path and generally longer residence time, or dilution with dead carbon produced by carbonate dissolution (Clark and Fritz, 1997), where a consequent isotopic exchange with the Cambrian carbonate matrix has occurred. It is worth mentioning that sample no. 16 has high $A^{14}C_{DIC}$ and low $\delta^{13}C_{DIC}$ values (−13.1‰) reflecting a mixture of high fraction modern water, and an important modern recharge with arrival of very "young" $^{14}C_{DIC}$ even related to the "nuclear epoch" (normally tritium-bearing groundwater), which is verified by the relatively lower values of water temperature and Cl^- concentration, and a relatively higher NO_3^- concentration (Table 1).

4.4. Geothermometry

The estimated temperatures of the thermal waters from the study area use the following geothermometers (Table 3 and Fig. 4): quartz

Table 3
Calculated reservoir temperatures using different geothermometers and circulation depth. The average temperature (T) is based on the quartz and improved SiO_2 geothermometers. The circulation depth is in km; all other values are in °C.

Sampling ID	Quartz geothermometer (Fournier, 1977)	improved SiO_2 (Verma and Santoyo, 1997)	Average T	K-Mg (Giggenbach, 1988)	Na-K (Giggenbach, 1988)	Na-K-Ca (Fournier and Truesdell, 1973)	Circulation depth
1	81.7	82.5	82.1	37.6	323	−24.4	3.1
2	115.4	115.7	115.5	67.7	1544	69.9	4.7
3	57.0	57.2	57.1	9.1	297	−8.2	2.0
4	83.9	84.7	84.3	40.1	425	−18.5	3.3
5	79.1	79.9	79.5	40.5	524	50.7	3.0
6	76.2	77.0	76.6	41.3	529	34.8	2.9
7	80.5	81.3	80.9	41.9	609	21.0	3.1
8	94.5	95.2	94.9	50.5	331	1.3	3.8
9	70.2	70.9	70.5	13.4	447	6.9	2.6
10	80.3	81.1	80.7	48.8	719	16.3	3.1
11	89.6	90.4	90.0	136.0	6025	413.9	3.5
12	74.3	75.0	74.6	82.4	24,869	366.1	2.8
13	73.6	74.4	74.0	82.9	24,011	367.8	2.8
14	66.6	67.1	66.8	107.5	18,619	501.6	2.4
15	53.8	53.7	53.8	120.1	24,834	525.8	1.8
16	37.0	35.1	36.1	69.1	13,846	457.6	0.9
17	48.3	47.7	48.0	79.4	7873	2158.0	1.5

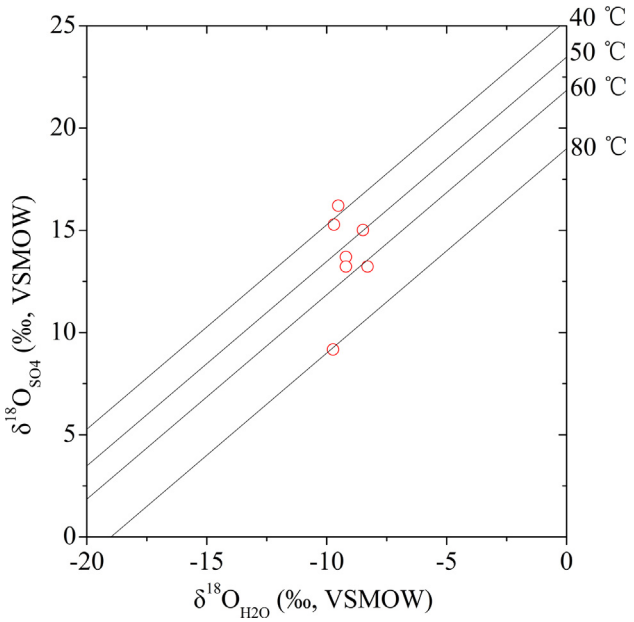

Fig. 4. Reservoir temperatures estimated by the $\delta^{18}O_{SO4\text{-}H2O}$ geothermometer.

geothermometer (Fournier, 1977), improved SiO_2 geothermometer (Verma and Santoyo, 1997), K-Mg geothermometer (Giggenbach, 1988), Na-K geothermometer (Giggenbach, 1988), Na-K-Ca geothermometer (Fournier and Truesdell, 1973), and $\delta^{18}O_{SO4\text{-}H2O}$ geothermometer (Lloyd, 1968). The estimated reservoir temperatures by the quartz geothermometer (Fournier, 1977) vary in the range of 37–90 °C (averaging at 63 ± 18 °C) for Group A, and 57–115 °C (averaging at 82 ± 15 °C) for Group B. The estimated temperatures measured by the improved SiO_2 geothermometer (Verma and Santoyo, 1997) are 35–90 °C (averaging at 63 ± 19 °C) for Group A, and 57–116 °C (averaging at 83 ± 15 °C) for Group B. The K-Mg geothermometer (Giggenbach, 1988) is indicative of the temperatures ranging from 69 to 136 °C, with an average of 97 ± 25 °C for Group A, and from 9 to 68 °C, with an average of 39 ± 17 °C for Group B. The geothermometers of Na-K (Giggenbach, 1988) and Na-K-Ca (Fournier and Truesdell, 1973) yield abnormal temperatures. The temperatures estimated by the $\delta^{18}O_{SO4\text{-}H2O}$ geothermometer of the seven selected thermal water samples from Group B vary from 39 to 80 °C (Fig. 4).

5. Discussion

5.1. Principal geochemical processes

Ionic ratios are useful in providing insight into the geochemical processes governing the water major ion chemistry (e.g. Marques et al., 2013; Yang et al., 2017). The ionic analysis makes it possible to conduct a preliminary screening of the geochemical reactions that occur in the thermal aquifers.

Dissolution of halite releases equal mole concentrations of Na^+ and Cl^- in the solution, and its corresponding reaction can be expressed as Eq. (1), in which a Na^+/Cl^- equivalent ratio approximately equaling to 1 as a result of the halite dissolution. The plot of Na^+ vs. Cl^- has been widely used to identify the mechanism of salinity (Dixon and Chiswell, 1992). The mmol/L ratio of Na^+ vs. Cl^- for all thermal waters plot around the 1:1 line (Fig. 5a), indicating that the Na^+ and Cl^- derive their salinity from the dissolution of halite within host sedimentary formations. Indeed, a drilling report in 1970 s showed that the Middle Cambrian carbonate aquifer within Group A was imbedded with a > 300 m salt depositing layer (GBSP, 1979). Moreover, the SIs values of halite are undersaturated (Table 2), indicating the thermal waters could dissolve more halite. The saline springs characterized by the hydrochemical facies of chloride sodium were widely found in the adjacent areas in Sichuan basin, as a result of dissolution of the halite formations (Guo et al., 2019). The existence of antecedent NaCl-type water can also be found in the thick, dominantly siliciclastic low-permeability confining layer of confined carbonates (Mádl-Szőnyi and Tóth, 2015).

$$NaCl \rightarrow Na^+ + Cl^- \quad (1)$$

The $(Ca^{2+} + Mg^{2+})$ vs. $(HCO_3^- + SO_4^{2-})$ can be employed to investigate the main geochemical processes (Fu et al., 2018). If these ions are controlled by carbonate and gypsum equilibrium, the equivalent ratio of $(Ca^{2+} + Mg^{2+})/(HCO_3^- + SO_4^{2-})$ would be a 1:1 relationship. All thermal water samples of the study are clustered closer to the 1:1 line (Fig. 5b), indicating that the dissolution of both carbonate and gypsum (and/or anhydrite) is the predominant hydrochemical process influencing water quality and is the main source of Ca^{2+}, Mg^{2+}, HCO_3^-, SO_4^{2-} (Fisher and Mullican, 1997). Chemically, the dissolution of limestone and dolomite are characterized by mmol/L ratios of 1:2 and 1:4 for Ca^{2+}/HCO_3^- and Mg^{2+}/HCO_3^-, respectively, expressed as Eqs. (2) and (3). However, the mmol/L ratios of Ca^{2+}/HCO_3^-, Mg^{2+}/HCO_3^- for most samples plot farther away from lines 1:2 (Fig. 5c) and 1:4 (Fig. 5d), respectively, suggesting that the Ca^{2+}, Mg^{2+} in the waters are not derived mainly from the dissolution of limestone and dolomite.

$$CO_2 + H_2O + CaCO_3 \rightleftharpoons Ca^{2+} + 2HCO_3^- \quad (2)$$

$$CaMg(CO_3)_2 + 2CO_2 + 2H_2O \rightleftharpoons Ca^{2+} + Mg^{2+} + 4HCO_3^- \quad (3)$$

The mmol/L ratios of Ca^{2+}/SO_4^{2-} of the thermal waters plot around the 1:1 line of the theoretical slope of a gypsum and/or anhydrite solution in equilibrium (Fig. 5e) as written by Eq. (4), which suggests that they are from the dissolution of evaporitic sulfate minerals. The SO_4^{2-} concentrations of Group A are two times higher than those of Group B (Table 1), because the solubility of gypsum is boosted with the presence of NaCl in solution, up to three times (Klimchouk, 2000). In addition, the HCO_3^- concentrations are not increasing with the elevating Ca^{2+} concentrations, with a negative relationship between them (Fig. 5c) and negative correlation between HCO_3^- and SO_4^{2-} (Fig. 5f), suggesting that the geochemical processes were controlled by the common ion effect as expressed by Eq. (5) which indicates dissolution of gypsum and/or anhydrite and forces calcite precipitation (Clark and Fritz, 1997; Jin et al., 2010). In Eq. (5), one mole of SO_4^{2-} is produced when gypsum and/or anhydrite dissolves, and two moles of HCO_3^- are lost as one mole of $CaCO_3$ forms. This effect was widely found in many carbonate hydrothermal systems (e.g. Yang et al., 2017, 2019).

$$CaSO_4{\cdot}nH_2O \rightarrow Ca^{2+} + SO_4^{2-} + nH_2O \quad (4)$$

$$2HCO_3^- + CaSO_4{\cdot}nH_2O \rightarrow CaCO_3\downarrow + CO_2\uparrow + SO_4^{2-} + (1+n)H_2O \quad (5)$$

where, the dissolution reaction for gypsum (n = 2) and anhydrite (n = 0).

It should be noted that the mean Mg^{2+} concentrations of Group A and Group B are 3.2 and 6.7 times higher than those of shallow karst groundwaters with a mean value of 13.8 mg/L reported by Pu et al. (2013), respectively. When dolomite is combined with the dissolution of gypsum and/or anhydrite in aquifers, the process of dedolomitization may take place, resulting in elevated concentrations of Mg^{2+} and SO_4^{2-}, and calcite precipitation (Appelo and Postma, 2005; Bischoff et al., 1994; Jacobson et al., 2010), expressed as Eq. (6). This type of reaction was described in other carbonate aquifers imbedded with evaporitic sulfates (gypsum and/or anhydrite), such as carbonate aquifers in Taiyuan, northern China (Ma et al., 2011), northeastern Spain (Bischoff et al., 1994), southwestern Oklahoma (Raines and Dewers, 1997), and southern Dakota, USA (Jacobson et al., 2010).

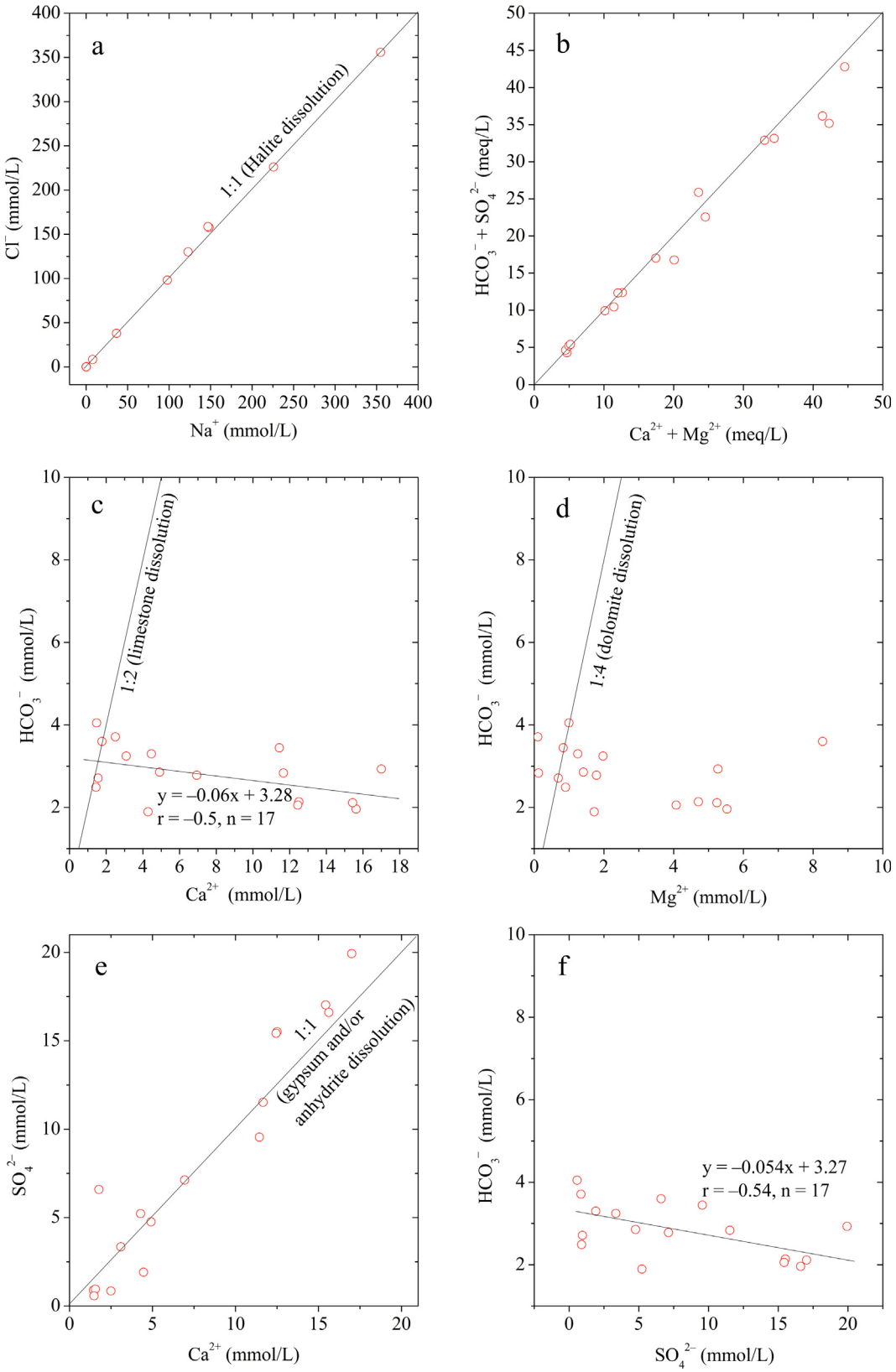

Fig. 5. Ionic ratio plots of the major ions: (a) Cl^-/Na^+, (b) $(HCO_3^- + SO_4^{2-})/(Ca^{2+} + Mg^{2+})$, (c) HCO_3^-/Ca^{2+}, (d) HCO_3^-/Mg^{2+}, (e) SO_4^{2-}/Ca^{2+}, and (f) HCO_3^-/SO_4^{2-} in the thermal waters from SEC.

Thus, the high Mg^{2+} concentrations coupled with the positive relationship between Mg^{2+} and SO_4^{2-} (r = 0.64, n = 17, not shown), and no obvious relationship between Mg^{2+} and HCO_3^- (Fig. 5d, n = 17), suggests that the Mg^{2+} in the thermal waters is derived from dedolomitization driven by the dissolution of gypsum and/or anhydrite rather than the dissolution of dolomite by CO_2. Raines and Dewers (1997) have reported that dedolomitization can occur only when gypsum approaches equilibrium under slow-flow conditions, when time

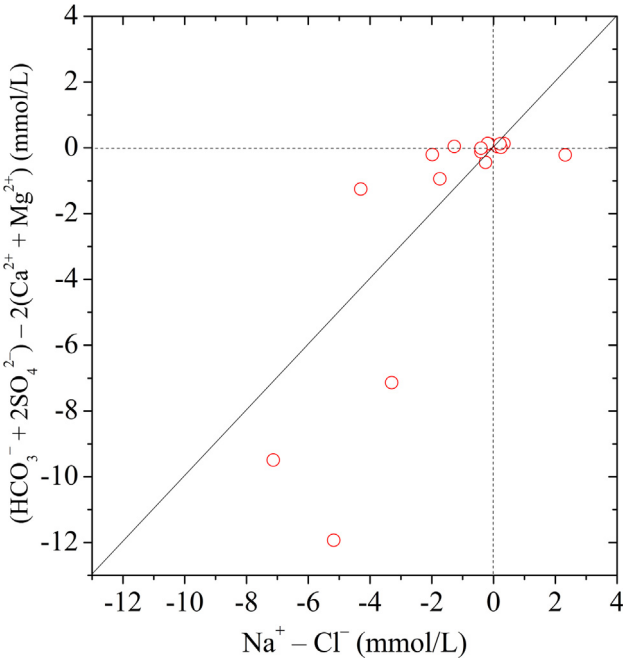

Fig. 6. Plot of $(Na^+ - Cl^-)$ vs. $[(2SO_4^{2-} + HCO_3^-) - 2(Ca^{2+} + Mg^{2+})]$ suggesting no cation exchange in the thermal waters in SEC.

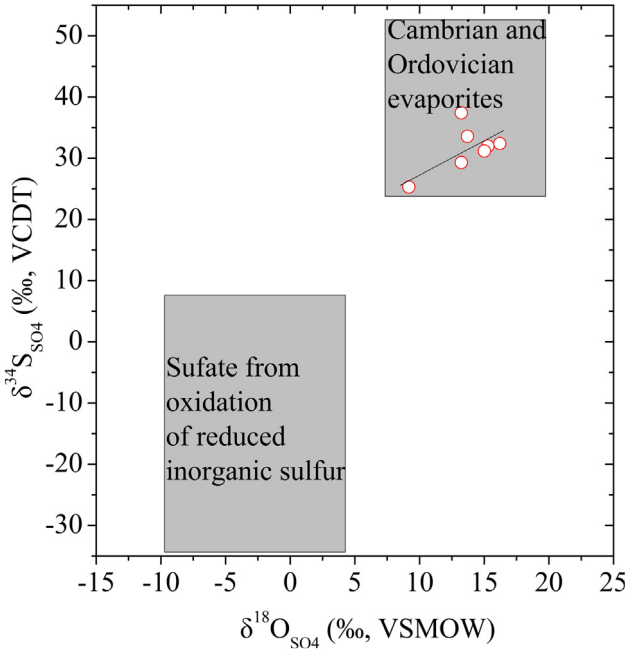

Fig. 7. A plot of $\delta^{34}S_{SO4}$ vs $\delta^{18}O_{SO4}$ suggests that the sulfate in the thermal waters is derived from the dissolution of Cambrian and Ordovician evaporites. The isotopic range from oxidation of reduced inorganic sulfur is adapted from Mayer and Krouse (2004), while the isotopic range of Cambrian and Ordovician evaporites is base on the data from Strauss (1997), Goldberg et al. (2005), Lu et al. (2018), and Claypool et al. (1980).

scales of the various mineral reaction rates approach each other.

$$CaMg(CO_3)_2 + CaSO_4{\cdot}nH_2O \rightarrow Mg^{2+} + SO_4^{2-} + 2CaCO_3\downarrow + nH_2O \quad (6)$$

where, the dissolution reaction for gypsum (n = 2) and anhydrite (n = 0).

The relationship between $(Na^+ - Cl^-)$ and $[(2SO_4^{2-} + HCO_3^-) - 2(Ca^{2+} + Mg^{2+})]$ (mmol/L) can determine whether cation (sodium-calcium) exchange occurs (Carol et al., 2009; Chen et al., 2014). If cation exchange dominates the geochemical processes, the relationship between the two parameters should be linear with a slope of 1. The $(Na^+ - Cl^-)$ vs. $[(2SO_4^{2-} + HCO_3^-) - 2(Ca^{2+} + Mg^{2+})]$ is plotted in Fig. 6, which shows that the samples are not distributed around the slope of 1. This suggests that the major cations do not participate in the cation exchange. Indeed, there are no feldspar, sodium-bearing minerals imbedded in the host carbonate rocks.

Since analysis of chemical compositions and ratio can only provide the concentration of sulfate and its potential source, but not its definite source, further analyses of isotopic $^{34}S_{SO4}$ and $^{18}O_{SO4}$ were carried out to decipher the origin of the sulfate content. Because SO_4^{2-} from different sources is characterized by distinct "fingerprints" (Clark and Fritz, 1997), the dual stable isotopes of sulfate have been widely employed to determine the origin of SO_4^{2-} in water, groundwater evolution and water-rock interactions occurring in groundwater (thermal) systems (e.g. González-Ramón et al., 2017; Grasby et al., 2000; Marques et al., 2013; Xiao et al., 2018). This approach was particularly successful when both the sulfur and oxygen isotope abundance ratios in the sulfate ion were determined.

Pu et al. (2013) found that the shallow karst groundwaters in the studied region ranged from 1.3 to 14‰ with an average of 6.2‰ for $\delta^{34}S_{SO4}$ and 6.7–45.1 mg/L with an average 19.6 mg/L for SO_4^2, and suggested multi-sulfur sources including atmospheric acid deposition, dissolution of gypsum, oxidation of sulfide mineral, and contributions from coal-containing strata or anthropogenic inputs. The $\delta^{34}S_{SO4}$ and SO_4^{2-} in the thermal waters of this study are many times higher than that of shallow groundwaters reported by Pu et al. (2013), suggesting that they are governed by different sulfur sources and different controlling mechanisms.

The SO_4^{2-} in the thermal waters could result from isotopic exchange in the system SO_4^{2-}–H_2S, sulfate reduction, sulfide oxidation, dissolution of evaporitic sulfate (gypsum and/or anhydrite), dissolution of sedimentary sulfides (i.e., pyrite). The $\delta^{34}S_{SO4}$ values of the thermal waters (Table 1 and Fig. 7) are among the range of $\delta^{34}S_{SO4}$ values in the seawater during Cambrian times (around 30‰; Strauss, 1997), near the values of 34 to 53‰ for phosphorites and carbonates within the Yangtze Platform, China (Goldberg et al., 2005), and similar to the range of 28.2 to 33.7‰ in Cambrian and Ordovician carbonate thermal waters of the Tangshan hydrothermal system near Nanjing, China (Lu et al., 2018). The $\delta^{18}O_{SO4}$ values of the thermal waters (from 9.2 to 16.2‰, averaging at 13.7 ± 2.3‰) are in agreement with published $\delta^{18}O_{SO4}$ values of 14‰ from Cambrian evaporitic calcium sulfates (Claypool et al., 1980) and correspond with isotopic compositions of marine sulfate with a range of 12 to 15‰ throughout the period of late Neoproterozoic to early Cambrian in Yangtze Platform, China (Goldberg et al., 2005). Moreover, the dissolution of gypsum or anhydrite occurs without measurable isotope effects relative to the evaporitic sulfate minerals (Clark and Fritz, 1997). Thus, in combination with the result of ionic ratios mentioned above, the SO_4^{2-} in the thermal waters are interpreted to be derived from the dissolution of gypsum and/or anhydrite formed in the Cambrian and Ordovician periods, which were found in the deeper regional formations within the aquifer (GBSP, 1979). Gypsum dissolution has produced significant tertiary porosity and permeability in the aquifers, which is an essential precursor to the development of karstic drainage (Gunn et al., 2006).

Although there is no evidence from the ionic ratios showing the dissolution of carbonate (limestone and/or dolomite), the HCO_3^- existing in the thermal waters firmly suggests that the dissolution of carbonate derived by CO_2 occurs, which is covered by the other hydrochemical processes mentioned above. Thus, the dissolution of carbonate, gypsum and/or anhydrite and halite, common ion effect, and dedolomitization mainly control the hydrochemical processes in the carbonate-evaporite thermal aquifers of SEC. The occurrence of these

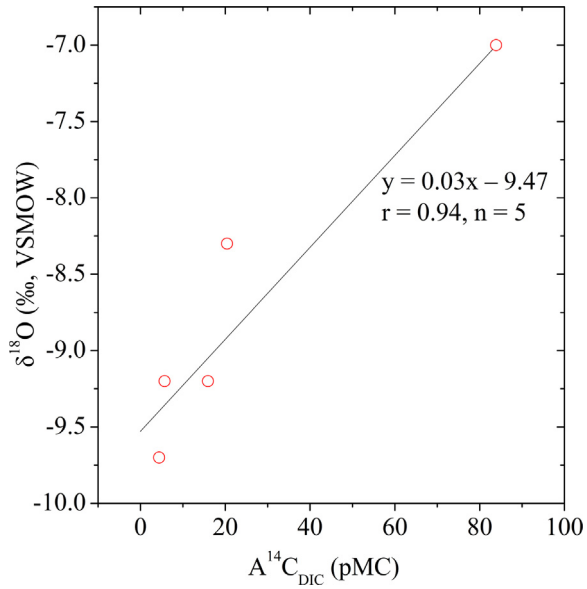

Fig. 8. Relationship between $\delta^{18}O$ and $A^{14}C_{DIC}$, indicating the more residence time, the more depleted ^{18}O in the thermal waters.

thermal waters, as well as their diverse chemical characteristics, seem to indicate that large-scale deep-seated groundwater flow systems exists in the karstic aquifers.

5.2. Origin of the thermal waters

The potential water origin can be traced using stable oxygen and hydrogen isotopes (Dansgaard, 1964). Except for sample no. 16, the thermal waters have mean values of −9.0, −59.8‰ for $\delta^{18}O$ and δD, respectively, and very isotopically depleted compared to the water samples from four rivers (Fig. 1) with a mean value of −6.3 and −38.5‰ for $\delta^{18}O$ and δD, respectively (unpublished data), suggesting a paleoclimatic signature in the thermal waters (Dansgaard, 1964; Fu et al., 2018; Huang et al., 2017a), and meaning that the recharging meteoric water was recharged at a relative wetter and colder climatic condition than present time. Except for sample no. 16, the corrected $A^{14}C_{DIC}$ dating of the thermal waters show that the average age is approximately 14.8 ka BP (see Section 5.4), corresponding to the late Pleistocene. This confirms the depleted ^{18}O and ^{2}H characteristics of the thermal waters. Thus, there is a positive relationship between $\delta^{18}O$ and $A^{14}C_{DIC}$ (Fig. 8), because the less $A^{14}C_{DIC}$ concentrations in the thermal waters, the more residence time and more negative $\delta^{18}O$ values are (Stute and Deak, 1989). Dansgaard (1964) has reported that the $\delta^{18}O$ and δD values show a positive correlation with the temperature with a slope of 0.69‰ per °C for $\delta^{18}O$ and 5.6‰ per °C for δD. From this information, it can be inferred that the thermal waters were recharged under a paleoclimate characterized by a mean of 3.8 °C colder than the present-day annual average temperature. This result is confirmed by many studies in China. For example, lower winter temperatures in the late Pleistocene as compared to modern times where demonstrated during a study of the mammalian fauna from a cave in the Three Gorges Area (Pang et al., 2017), approximately 200 km north away from the study area; and the recharge temperatures in the late Pleistocene of about 2–3 °C cooler than the modern mean annual air temperature within the Minqin Basin, NW China (Edmunds et al., 2006).

Among the thermal waters, the isotopic enrichment of ^{18}O and ^{2}H of sample no. 16 is associated with recent "younger" water recharge, which is confirmed by high $A^{14}C_{DIC}$ (as mentioned in Sections 4.3 and 5.4).

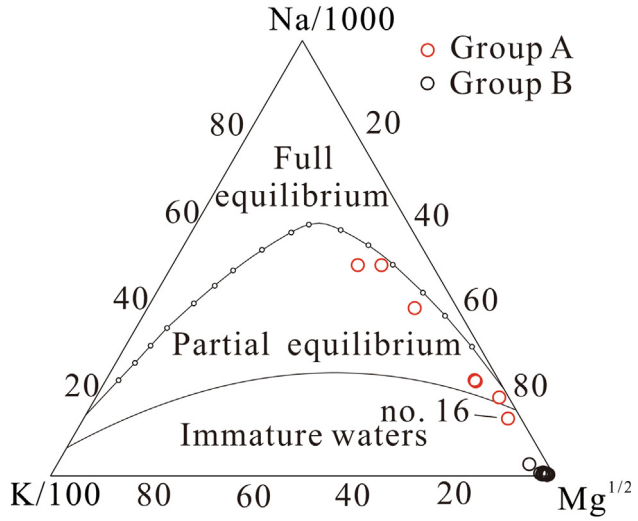

Fig. 9. Na-K-Mg Giggenbach plot of the thermal waters hosted by the fault area within SEC.

5.3. Reservoir temperature and circulation depth

The Na-K-Mg triangular plot proposed by Giggenbach (1988) was introduced as a powerful tool in the interpretation of geothermal geochemistry. In this plot, waters are divided into three groups, including fully equilibrated water, partially equilibrated water, and immature water, allowing a clear distinction to be made between waters suitable or unsuitable for the application of cation geothermometers (Giggenbach, 1988). The thermal waters of the study area are superposed on the Na-K-Mg Giggenbach plot shown in Fig. 9. Except for sample no. 16, the thermal waters of Group A are located at the partially equilibrated zone, whereas the samples of Group B plot near to the Mg^{2+} corner and correspond to immature waters. This suggests that the ascending deep-seated thermal fluids of Group B along with sample no. 16 are mixing with cold water and/or re-equilibrating along their circulation and thus unsuitable for the evaluation of cation equilibration. Moreover, in a sedimentary environment, the mineralogy of the host rocks and the low prevailing temperatures (< 150 °C) lead to slow kinetics, with the result that cation solute geothermometers based on equilibrium with K-feldspars and Ca-bearing silicates cannot be applied (Levet et al., 2006). Hence, all the temperatures given by the cation solute geothermometers are baseless, which are characterized by unrealistically high or negative equilibration temperatures (Table 3).

Most SIs of the thermal waters are undersaturated except for the quartz values which are oversaturated (Table 2), which suggests that the quartz equilibrium is established between the thermal waters and host rock. So, the silica geothermometers may be most suitable for the thermal waters from the study area. Best-estimated temperatures by the quartz geothermometer (Fournier, 1977), and improved SiO_2 geothermometer (Verma and Santoyo, 1997) average at 63 ± 18 °C and 63 ± 19 °C for Group A, and average at 82 ± 15 °C and 83 ± 15 °C for Group B. The estimated temperatures by these two geothermometers yield similar results and are within the uncertainty range of ± 20 °C, which is generally acceptable in geothermometrical calculations (Tole et al., 1993), and are consistent with estimated temperatures averaging at 80 °C based on a chemical thermodynamic model (unpublished data). The classical chemical geothermometers including silica geothermometers provide good results in high temperature (> 180 °C) systems hosted in rocks with feldspars and aluminosilicates with which the waters have reached equilibrium, and these geothermometers sometimes are not expected to be suitable for low-temperature and/or carbonate-evaporite aquifers in some cases (Blasco et al., 2018; Fournier and Truesdell, 1973). However, they can provide

rational, consistent and verified results in some low-and medium-temperature cases of carbonate systems (Bozdag, 2016; Renac et al., 2009; Yang et al., 2017), and serve as a reliable estimation of the reservoir temperature for thermal waters with high cation concentrations (Shestakova and Guseva, 2018). As such, the reservoir temperatures estimated by silica geothermometers in the study should be applicable and reliable.

Most of the temperatures of Group B estimated by $\delta^{18}O_{SO4\text{-}H2O}$ geothermometer are between 50 and 60 °C (Fig. 4), with one up to 80 °C. These results seem to be a little lower than those temperatures calculated by silica geothermometers reported above, probably implying an isotopic disequilibrium between $\delta^{18}O_{SO4}$ and $\delta^{18}O_{H2O}$ for low-temperature reservoirs. There are likely two reasons contributing to the isotopic disequilibrium. The first one, the ascending deep-seated thermal fluids mix with the shallow groundwater characterized by lower concentration SO_4^{2-} and enriched $^{18}O_{H2O}$. The second one, the exchange rates of oxygen isotope in the sulfate-water system are extremely slow. At earth-surface conditions it requires up to 100,000 years to approach near isotopic oxygen equilibrium between dissolved sulfate and water (Lloyd, 1968). Hence, the $\delta^{18}O_{SO4\text{-}H2O}$ geothermometer probably does not reflect the real reservoir temperature.

Moreover, the water oxygen signature from the thermal springs does not show an enrichment of ^{18}O (positive $\delta^{18}O$ shift) with respect to that of the regional and global meteoric water (Fig. 3). As meteoric water infiltrates through the ground into the geothermal reservoir, isotopic equilibrium with the surrounding rock matrix and the extent of isotopic exchange are controlled by the temperature (Geyh, 2001). Isotopic exchange of oxygen isotopes between the meteoric water and the carbonate or silicate formations with unchanged hydrogen isotope in high temperature aquifers was widely documented around the world (e.g. Gat, 2010; Tian et al., 2018; Wang et al., 2016). However, the water-rock interaction has little effect on $\delta^{18}O$ in groundwater at reservoir temperatures < 90 °C (Mook, 2000). The lack of positive $\delta^{18}O$ shift for the thermal waters within SEC implies that the reservoir temperature should be < 90 °C, which strangely suggests that the mean temperatures estimated by silica geothermometers are rational, compared to the temperatures estimated by other chemical geothermometers.

The maximum circulation depth of the thermal waters can be calculated by an equation shown in Eq. (7). The estimated reservoir temperature (*t*) is set to the average temperature estimated by the two silica geothermometers, including the quartz geothermometer (Fournier, 1977), and improved SiO_2 geothermometer (Verma and Santoyo, 1997). The local mean annual air temperature (t_0) is 16.6 °C. The depth of constant temperature zone (*d*) is assumed to be 0.03 km according to Yang et al. (2019). The geothermal gradient (*g*) is from the average value calculated by an equation as expressed by Eq. (8). The bottom-hole temperature (t_b), and the well depth (d_w) in km are listed in Table 4. Thus, the calculated *g* values of samples nos. 3, 5 and 12 (drilled wells) are 22.9, 21.1, and 19.5 °C/km, respectively (Table 4), with an average of 21 °C/km, slightly below the average of the earth crust (30 °C/km). These values are consistent with the thermal anomaly described in this area with an average geothermal gradient value of < 25 °C/km (Chen, 1994). The reservoir temperatures by silica geothermometers in conjunction with the average geothermal gradient of 21 °C/km indicate that the circulation depth ranges from 1.5 to 3.5 km with an average of 2.5 ± 0.7 km for Group A except for sample no. 16, and 2 to 4.7 km with an average of 3.2 ± 0.7 km for Group B. Although these values cannot be confirmed or rejected, they are the most reliable data for the study area.

$$D = (t - t_0)/\, g + d \quad (7)$$

where, *D* is the circulation depth in km; *t* is the estimated reservoir temperature in °C; t_0 the local mean annual air temperature in °C; *g* is the geothermal gradient in °C/km; and *d* is the depth of constant temperature zone in km.

$$g = (t_b - t_0)/d_w \quad (8)$$

where, *g* and t_0 are same as in Eq. (7); t_b is the bottom-hole temperature in °C; d_w is the well depth in km.

Table 4
Geothermal gradient of the thermal drilled wells within SEC. The meaning and units of dw, tb, and *g* are same as in Eqs. (7) and (8).

Sampling ID	d_w	t_b	g
3	1.645	54.23	22.9
12	1.866	56	21.1
13	1.455	45	19.5

5.4. Residence time of the thermal waters

Estimating groundwater age is important and useful for any groundwater resource assessment. Because numerous studies have reported that the carbonate thermal waters are more than several thousands of years old (Ettayfi et al., 2012; Mao et al., 2018; Yang et al., 2017), the $A^{14}C_{DIC}$ concentrations rather than the tritium dating of the thermal water samples were measured in this study. The half-life of 5730 years for $A^{14}C_{DIC}$ makes it highly useful for dating carbon-bearing materials allowing measurement to almost 60,000 years, which is considered to be a universal and reliable groundwater dating method (Clark and Fritz, 1997), and provides information and facilitates studies of archeological materials (Goldscheider and Drew, 2007; Meredith et al., 2016) and groundwater recharge mechanism (Huang et al., 2017b; Kulongoski et al., 2008).

In addition to radioactive decay, the $A^{14}C_{DIC}$ content can be affected by many geochemical and physical processes (Han et al., 2014), which controls the isotope geochemistry of carbon during water infiltration through the unsaturated zone (interactions in an open system) and within the aquifer system itself (interactions in a closed system) (Kattan, 2002). During transit in the aquifer, these processes modify the initial $A^{14}C_{DIC}$ content ($^{14}C_0$) in groundwater because the ancient rocks are free of $A^{14}C_{DIC}$ (dead carbon) which inevitably increases the calculated groundwater ages without correction. The measured $A^{14}C_{DIC}$ contents thus should be reassessed during the use of radiocarbon dating for thermal groundwater if additional dead carbon exists in the water (Aquilina et al., 2003; Mao et al., 2018). There is a negative relationship between $\delta^{13}C_{DIC}$ and $A^{14}C_{DIC}$ of the thermal waters within SEC (Fig. 10), which may suggest additional dead carbon. Thus, it's necessary to correct the ages of the thermal water samples of the SEC based on the measured $A^{14}C_{DIC}$.

The vegetation in the study area is dominated by C3 (Calvin C3 photosynthesis cycle). The $\delta^{13}C$ values of most C3 range from −24‰ to −30‰, with an average of −27‰ (Vogel, 1993). Due to the high concentration gradient, the degassing of soil CO_2 makes the $^{13}C_{CO2}$ fractionation as much as ~4‰ (Cerling et al., 1991; Jin et al., 2014). Thus, the $\delta^{13}C_{CO2}$ in the soil should be −23‰. When the soil CO_2 dissolved the carbonate aquifer, half of the DIC in aquifer is from the soil, and the other half is derived from the host carbonate rocks which results in an enrichment factor (ε) of $\delta^{13}C_{DIC}$ with an $\varepsilon^{13}C_{DIC\text{-}CO2(g)}$ value of ~9‰ at 15 °C (Clark and Fritz, 1997). Hence the $\delta\ ^{13}C_{DIC}$ as a result of C3 plants in the carbonate aquifer should be −14‰ at 15 °C. On the basis of these assumptions, a mixing model was proposed as shown in Fig. 10, in which the DIC in the thermal waters is a result of mixture of the dissolution of Cambrian carbonates in the thermal reservoir ($\delta^{13}C_{DIC}$ = ~0‰, $A^{14}C_{DIC}$ = 0 pMC) and CO_2 from soil respiration ($\delta^{13}C_{DIC}$ = −14‰ at 15 °C, $A^{14}C_{DIC}$ = 100 pMC).

Numerous calibrated models have been employed to estimate the radiocarbon ages of DIC in groundwater systems (e.g. Evans et al., 1979; Han et al., 2014; Huang et al., 2017a; Tamers, 1975). Generally, these models can be categorized into two types; processes of chemical

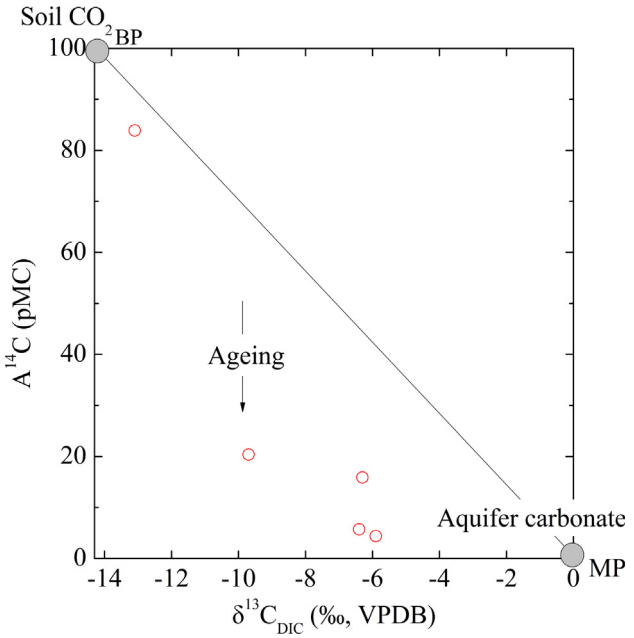

Fig. 10. The negative relationship between $\delta^{13}C_{DIC}$ and $A^{14}C_{DIC}$ of the thermal waters within SEC, showing two sources, including the aquifer carbonate with a high $\delta^{13}C_{DIC}$ value, and soil CO_2 with a low $\delta^{13}C_{DIC}$ value.

and isotopic mixing, and chemical mixing with isotopic exchange (Clark and Fritz, 1997). However, the calculated $\delta^{13}C_{CO2}$ values in the thermal waters range from −5.7‰ to −20.7‰ (averaging at −12.7‰) based on a linear regression between $\delta^{13}C_{DIC}$ and $\delta^{13}C_{CO2}$ as expressed by Eq. (9) from Deines et al. (1974). Except for samples nos. 16 (−20.7‰) and 17 (−19.0‰), most of the calculated $\delta^{13}C_{CO2}$ values of the thermal waters are much higher than that of the theoretical value in the soil (−23‰). The higher $\delta^{13}C_{CO2}$ values together with the higher $\delta^{13}C_{DIC}$ values of the thermal waters suggest that the solutions in the thermal aquifers occur chiefly under closed groundwater systems, which is confirmed by the "isolated" thermal aquifers based on the lower nitrate concentrations compared with those of the shallow karst groundwaters reported by Pu et al. (2013). A widely used correction model, ALK model (Tamers, 1975), was employed to correct the ages in this study. Because this model is based on initial and final carbonate (DIC) concentrations, and was proposed for groundwater in which calcite is dissolved under closed system conditions. Moreover, this model assumes fully closed system conditions without exchange of soil CO_2 during calcite dissolution (Tamers, 1975). The corrected ages by the ALK model are listed in Table 1. Generally, most of the corrected $^{14}C_{DIC}$ ages (n = 5) are much younger than the uncorrected $^{14}C_{DIC}$ ages. Except for sample no.16, the corrected ages are from 9 to 21 ka BP, with an average of 14.8 ka BP. The corrected age of sample no. 16 is negative and irrational because of mixture with younger water. Although the corrected $^{14}C_{DIC}$ ages may deviate from the real ages to some extent, it is believed to be more accurate than the uncorrected ages and can indicate the age level of the thermal waters.

$$\delta^{13}C_{CO2} = \delta^{13}C_{DIC} + 4.54 - 1.099 \times 10^6/T^2 \quad (9)$$

where, T is the temperature of thermal water in Kelvin degree.

The estimation of renewable groundwater resources and understanding of related hydrological processes are critically dependent upon determining the presence and age of modern groundwater (Aggarwal, 2002). Deep groundwater characterized by more than 1 ka ages is considered non-renewable paleo water, without the possibility of significant replenishment under present climatic conditions (Huang et al., 2017a). Generally, the depletion of $\delta^{18}O$ and δD in the thermal waters compared to modern recharge, coupled with the low $A^{14}C_{DIC}$ concentrations and their corresponding corrected ages suggest that the renewability rate for most of the thermal water resources in the aquifers is characterized by a hydraulic continuity on an order of ~14.8 ka. Thus, aquifer renewability needs to be fully considered and assessed before groundwater exploitation and extraction.

5.5. Conceptual circulation of the thermal waters

According to the hydrogeochemical and geothermometrical results above, a conceptual hydrogeological model was reconstructed as schematically depicted in Fig. 11, which is a qualitative, schematic representation of (or part of) reality. The poorly known or unknown characteristics of the hydrothermal aquifer systems of interest, such as the precise location of the infiltration areas as well as the geometry of the geological bodies hosting most of the hydrogeological flow path, are roughly shown in Fig. 11.

The thermal waters originate from common meteoric water at a relative wetter and colder climate in the late Pleistocene. Assuming a geothermal gradient of 21 °C/km, the meteoric water infiltrates into the subsurface at maximum depth at roughly 2.5 and 3.2 km for Group A and Group B, respectively, to acquire the heat from deep rock through conductive transfer during their circulation and form the deep-seated thermal fluids characterized by temperatures of approximately 63 and 83 °C for Group A and Group B, respectively. The fluids are characterized by cross-formational hydraulic continuity. At the same time, the

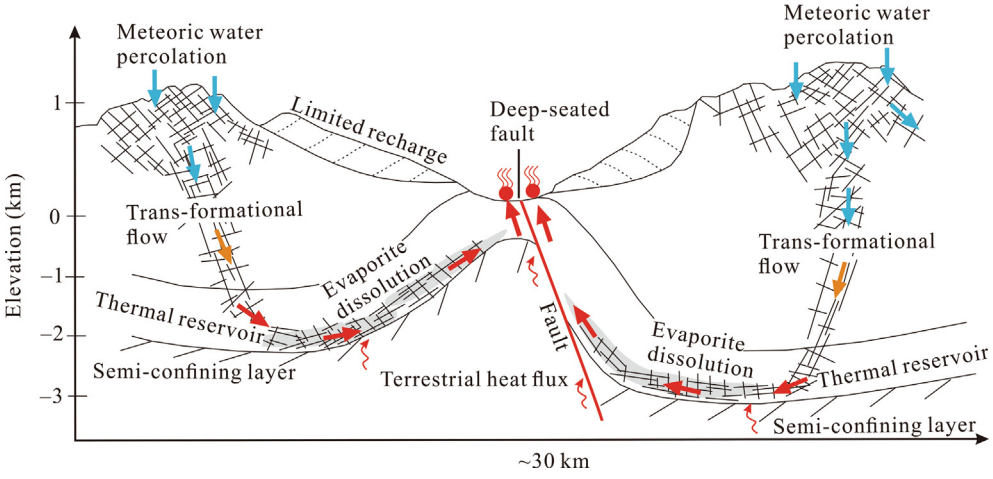

Fig. 11. Conceptual hydrogeological model of the formation for hydrothermal systems within SEC, in which the arrows indicate flow direction, and blue to red colors show cold to hot water temperatures. The Meteoric water infiltrates deeply into the carbonate-evaporite rocks and extracts heat from the rocks resulting in deep-seated thermal fluids. The fluids gain salinity by interaction with the evaporitic deposits. The origin of the hot springs is due to deep-ground water circulation controlled by faults in the subsurface reservoir. The thermal flow is primarily driven by topographic head difference between the recharge area and the hot springs. Free thermal convection can take place in the deeper part of the hydrothermal systems. (For interpretation of the references to colour in this figure legend, the reader is referred to the web version of this article.)

fluids interact with evaporitic deposits composed of halite and sulfate minerals at depth, which results in high salinity, particularly the enrichment of Na^+ and Cl^- in Group A. The fluids returning flow to the surface is mainly driven by topographic head difference (Tóth, 1963) between the recharge area in the limestone mountains and the thermal water resurgences. Free thermal convection may affect the deeper part of the midline and the discharge zone of the hydrothermal systems as well (Szijártó et al., 2019). The local tectonic setting represented by the presence of the deep-seated faults in this area enhances the permeability and plays an important role in the circulation and upwelling of deep-seated thermal fluids toward the surface. The deep-seated thermal fluids move up along the faults and mix with different proportions of colder waters to form the hot springs. This mixing accounts for the variations in temperatures and chemical compositions among individual springs or drilled well waters, such as sample no. 16 characterized by a high mixture fraction of modern water. There are possible similar hydrologic environments between Group A and Group B indicated by the chemical identification, but there are differences in the halite imbedded in the aquifers and circulation depths between the two groups.

Although the mechanism of the geothermal flow dynamics to some extent remains speculative, the conceptual hydrogeological model is the most rational based on the analyses of hydrogeological settings, and the hydrogeochemical and geothermometrical data.

6. Conclusions

This paper is the first to present the hydrogeochemistry and geothermometry of the thermal waters from carbonate-evaporite aquifers hosted by deep-seated faults in Southeast Chongqing, China, where thermal fluids discharge from Cambrian and Ordovician carbonate-evaporite rocks, representing the main potential thermal reservoir.

Major ions and isotopes ($^{34}S_{SO4}$, $^{18}O_{SO4}$, ^{18}O, ^{2}H, $^{13}C_{DIC}$, and $A^{14}C_{DIC}$) were employed to constrain the hydrogeochemistry and geothermometry of the thermal waters from carbonate-evaporite aquifers hosted by deep-seated faults in the study area. The low-temperature hydrothermal systems are manifested by hot springs emerging around the faults. The groundwater interaction with carbonate-evaporite rocks explains the two distinct chemical compositions of the thermal waters characterized by the chloride sodium waters with higher TDS (Group A), and sulfate-bicarbonate-chloride alkaline-earth waters with relative lower TDS (Group B) in the study area. The dissolution of carbonate, gypsum and/or anhydrite and halite, common ion effect, and dedolomitization control the hydrochemical processes in the carbonate-evaporite thermal aquifers. The thermal waters originate from meteoric water. The reservoir temperature appears to be 63 ± 18 °C for Group A and 82 ± 15 °C for Group B, as indicated by silica geothermometers. The corrected $^{14}C_{DIC}$ ages average at 14.8 ka BP, corresponding to late Pleistocene, which suggests that the renewability rate of most of the thermal waters are on an order of ~14.8 ka. Thus, the slow renewability rate of thermal water resources in the study area inevitably provides a challenge to the future utilization for social and economic development.

Monitoring the major ions and isotopic compositions of thermal waters can provide important indications as to the formational mechanisms of the carbonate-evaporite hydrothermal systems. Indeed, such monitoring provides valuable information of the thermal waters to define the hydrogeochemistry and geothermometry of the aquifers, and lays a solid foundation for future efficient utilization, management, and implementation of water conservation policies for the thermal water resources in the study area. The methodological approachs utilized in this research may also be applied to other fault-controlled, low-temperature carbonate hydrothermal systems in other non-volcanic zones of China and other nations.

Declaration of Competing Interest

The authors declare that they have no known competing financial interests or personal relationships that could have appeared to influence the work reported in this paper.

Acknowledgments

The authors thank Tianming Huang and Yinlei Hao from the Institute of Geology and Geophysics, Chinese Academy Sciences, and the anonymous reviewers for their constructive and valuable comments. This work was financially supported by the Fundamental Research Funds for the Central Universities (Grant no. XDJK2018AB002), the Chongqing Research Program of Basic Research and Frontier Technology (Grant nos. cstc2019jcyj-msxmX0062, cstc2016jcyjA0921) and the China Scholarship Council.

References

Adam, P., Jan, D., 2009. Application of selected geothermometers to exploration of low-enthalpy thermal water: the Sudetic Geothermal Region in Poland. Environ. Geol. 58 (8), 1629–1638. https://doi.org/10.1007/s00254-008-1409-7.

Aggarwal, P.K., 2002. Isotope hydrology at the International Atomic Energy Agency. Hydrol. Process. 16 (11), 2257–2259. https://doi.org/10.1002/hyp.5043.

Appelo, C.A.J., Postma, D., 2005. Groundwater and Pollution, second ed. A.A. Balkema Publishers, Leiden.

Aquilina, L., Ladouche, B., Doerfliger, N., Bakalowicz, M., 2003. Deep water circulation, residence time, and chemistry in a karst complex. Ground Water 41 (6), 790–805. https://doi.org/10.1111/j.1745-6584.2003.tb02420.x.

Awaleh, M.O., Hoch, F.B., Boschetti, T., Soubaneh, Y.D., Egueh, N.M., Elmi, S.A., Mohamed, J., Khaireh, M.A., 2015. The geothermal resources of the Republic of Djibouti – II: geochemical study of the Lake Abhe geothermal field. J. Geochem. Explor. 159, 129–147. https://doi.org/10.1016/j.gexplo.2015.08.011.

Bischoff, J.L., Juliá, R., Shanks, W.C., Rosenbauer, R.J., 1994. Karstification without carbonic acid: bedrock dissolution by gypsum-driven dedolomitization. Geology 22, 995–998. https://doi.org/10.1130/0091-7613(1994) 022<0995:KWCABD>2.3.CO;2.

Blasco, M., Auqué, L.F., Gimeno, M.J., Acero, P., Asta, M.P., 2017. Geochemistry, geothermometry and influence of the concentration of mobile elements in the chemical characteristics of carbonate-evaporitic thermal systems. The case of the Tiermas geothermal system (Spain). Chem. Geol. 466, 696–709. https://doi.org/10.1016/j.chemgeo.2017.07.013.

Blasco, M., Gimeno, M.J., Auque, L.F., 2018. Low temperature geothermal systems in carbonate-evaporitic rocks: Mineral equilibria assumptions and geothermometrical calculations. Insights from the Arnedillo thermal waters (Spain). Sci. Total. Environ. 615, 526–539. https://doi.org/10.1016/j.scitotenv.2017.09.269.

Bouchaou, L., Warner, N.R., Tagma, T., Hssaisoune, M., Vengosh, A., 2017. The origin of geothermal waters in Morocco: multiple isotope tracers for delineating sources of water-rock interactions. Appl. Geochem. 84, 244–253. https://doi.org/10.1016/j.apgeochem.2017.07.004.

Bozdag, A., 2016. Hydrogeochemical and isotopic characteristics of Kayak (Seydisehir-Konya) geothermal field, Turkey. J. Afr. Earth Sci. 121, 72–83. https://doi.org/10.1016/j.jafrearsci.2016.05.019.

Carol, E., Kruse, E., Mas-Pla, J., 2009. Hydrochemical and isotopical evidence of ground water salinization processes on the coastal plain of Samborombon Bay, Argentina. J. Hydrol. 365 (3–4), 335–345. https://doi.org/10.1016/j.jhydrol.2008.11.041.

Carpenter, A.B., 1977. Origin and chemical evolution of brines in sedimentary basins. In: Johnson, K.S., Russell, J.A. (Eds.), Thirteenth Annual Forum on the Geology of Industrial Minerals. Norman, Oklahoma, pp. 60–77.

Cerling, T.E., Solomon, D.K., Quade, J., Bowman, J.R., 1991. On the isotopic composition of carbon in soil carbon dioxide. Geochim. Cosmochim. Acta 55 (11), 3403–3405. https://doi.org/10.1016/0016-7037(91)90498-T.

Chen, M.X., 1994. Geothermal Resource in China: Formational Characteristics and Potential Evaluation. Science Press, Beijing (in Chinese).

Chen, L., Wang, G., Hu, F., Wang, Y., Liu, L., 2014. Groundwater hydrochemistry and isotope geochemistry in the Turpan Basin, northwestern China. J. Arid Land 6 (4), 378–388. https://doi.org/10.1007/s40333-013-0249-9.

Chenaker, H., Houha, B., Vincent, V., 2018. Hydrogeochemistry and geothermometry of thermal water from northeastern Algeria. Geothermics 75, 137–145. https://doi.org/10.1016/j.geothermics.2018.04.009.

Clark, I., Fritz, P., 1997. Environmental Isotopes in Hydrogeology. Lewis Publishers, New York.

Claypool, G.E., Holser, W.T., Kaplan, I.R., Sakai, H., Zak, I., 1980. The age curves of sulfur and oxygen isotopes in marine sulfate and their mutual interpretation. Chem. Geol. 28 (3–4), 199–260. https://doi.org/10.1016/0009-2541(80)90047-9.

Craig, H., 1961. Isotopic variations in meteoric waters. Science 133 (3465), 1702–1703. https://doi.org/10.1126/science.133.3465.1702.

D'Amore, F., Arnórsson, S., 2000a. Sampling of geothermal fluids: on-site measurements and sample treatment. In: Arnórsson, S. (Ed.), Isotopic and Chemical Techniques in Geothermal Exploration. IAEA, Vienna, pp. 84–96.

D'Amore, F., Arnórsson, S., 2000b. Geothermometery. In: Arnórsson, S. (Ed.), Isotopic and Chemical Techniques in Geothermal Exploration, Development and Use. IAEA, Austria.
Dansgaard, W., 1964. Stable isotopes in precipitation. Tellus 16 (4), 436–468.
Deines, P., Langmuir, D., Harmon, R.S., 1974. Stable carbon isotope ratios and the existence of a gas phase in the evolution of carbonate waters. Geochim. Cosmochim. Acta 38, 1147–1164. https://doi.org/10.1016/0016-7037(74)90010-6.
Dixon, W., Chiswell, B., 1992. The use of hydrochemical sections to identify recharge areas and saline intrusions in alluvial aquifers, Southeast Queensland, Australia. J. Hydrol. 135 (1–4), 259–274. https://doi.org/10.1016/0022-1694(92)90091-9.
Dobson, P., Gasperikova, E., Spycher, N., Lindsey, N.J., Guo, T.R., Chen, W.S., Liu, C.H., Wang, C.J., Chen, S.N., Fowler, A.P.G., 2018. Conceptual model of the Tatun geothermal system, Taiwan. Geothermics 74, 273–297. https://doi.org/10.1016/j.geothermics.2018.01.001.
Edmunds, W.M., Ma, J., Aeschbach-Hertig, W., Kipfer, R., Darbyshire, D.P.F., 2006. Groundwater recharge history and hydrogeochemical evolution in the Minqin Basin, North West China. Appl. Geochem. 21 (12), 2148–2170. https://doi.org/10.1016/j.apgeochem.2006.07.016.
Ettayfi, N., Bouchaou, L., Michelot, J.L., Tagma, T., Warner, N., Boutaleb, S., Massault, M., Lgourna, Z., Vengosh, A., 2012. Geochemical and isotopic (oxygen, hydrogen, carbon, strontium) constraints for the origin, salinity, and residence time of groundwater from a carbonate aquifer in the Western Anti-Atlas Mountains, Morocco. J. Hydrol. 438–439, 97–111. https://doi.org/10.1016/j.jhydrol.2012.03.003.
Evans, G.V., Otlet, R.L., Downing, R.A., Monkhouse, R.A., Rae, G., 1979. Some Problems in the Interpretation of Isotope Measurements in United Kingdom Aquifers. IAEA, Vienna, pp. 679–706.
Fisher, R.S., Mullican, W.F., 1997. Hydrochemical evolution of sodium-sulfate and sodium-chloride groundwater beneath the Northern Chihuahuan Desert, Trans-Pecos, Texas, USA. Hydrogeol. J. 5 (2), 4–16. https://doi.org/10.1007/s100400050102.
Fournier, R.O., 1977. Chemical geothermometers and mixing models for geothermal systems. Geothermics 5 (1–4), 41–50. https://doi.org/10.1016/0375-6505(77)90007-4.
Fournier, R.O., Truesdell, A.H., 1973. An empirical Na-K-Ca geothermometer for natural waters. Geochim. Cosmochim. Acta 37, 1255–1275. https://doi.org/10.1016/0016-7037(73)90060-4.
Fournier, R.O., Truesdell, A.H., 1974. Geochemical indicators of subsurface temperature-2. Estimation of temperature and fraction of hot water mixed with cold water. U.S. Geol. Survey J. Res 2 (3), 263–270.
Fu, C., Li, X., Ma, J., Liu, L., Gao, M., Bai, Z., 2018. A hydrochemistry and multi-isotopic study of groundwater origin and hydrochemical evolution in the middle reaches of the Kuye River basin. Appl. Geochem. 98, 82–93. https://doi.org/10.1016/j.apgeochem.2018.08.030.
Gat, J., 2010. Isotope Hydroglogy: A Study of the Water Cycle. Imperial College Press, Singapore.
GBSP (Geological Bureau of Sichuan Province), 1979. Regional Hydrogeological Survey Report of Youyang (scale 1:200,000) (in Chinese).
Geyh, M., 2001. Groundwater saturated and unsaturated zone. In: Mook, W.G. (Ed.), Envrionmental isotopes in the hydrological cycle: Principles and Applications. IAEA.
Giggenbach, W.F., 1988. Geothermal solute equilibria. Dervivation of Na-K-Mg-Ca geoindicators. Geochim. Cosmochim. Acta 52 (12), 2749–2765. https://doi.org/10.1016/0016-7037(88)90143-3.
Goldberg, T., Poulton, S.W., Strauss, H., 2005. Sulphur and oxygen isotope signatures of late Neoproterozoic to early Cambrian sulphate, Yangtze Platform, China: Diagenetic constraints and seawater evolution. Precamb. Res. 137 (3–4), 223–241. https://doi.org/10.1016/j.precamres.2005.03.003.
Goldscheider, N., Drew, D., 2007. Methods in Karst Hydrogeology. Taylor & Francis, London, UK.
Goldscheider, N., Mádl-Szőnyi, J., Erőss, A., Schill, E., 2010. Review: thermal water resources in carbonate rock aquifers. Hydrogeol. J. 18 (6), 1303–1318. https://doi.org/10.1007/s10040-010-0611-3.
González-Ramón, A., López-Chicano, M., Gázquez, F., Durán-Valsero, J.J., Pedrera, A., Ruiz-Constán, A., González-Egea, E., 2017. Isotopic and hydrochemistry spatial variation of sulfate for groundwater characterization in karstic aquifers. Hydrol. Process. 31 (18), 3242–3254. https://doi.org/10.1002/hyp.11255.
Grasby, S.E., Hutcheon, I., Krouse, H.R., 2000. The influence of water-rock interaction on the chemistry of thermal springs in western Canada. Appl. Geochem. 15 (4), 439–454. https://doi.org/10.1016/S0883-2927(99)00066-9.
Gunn, J., Bottrell, S.H., Lowe, D.J., Worthington, S.R.H., 2006. Deep groundwater flow and geochemical processes in limestone aquifers: evidence from thermal waters in Derbyshire, England, UK. Hydrogeol. J. 14 (6), 868–881. https://doi.org/10.1007/s10040-006-0022-7.
Guo, J., Zhou, X., Zhang, Y., Ta, M., Wang, Y., 2019. Occurrence and hydrochemical characteristics of saline and salty springs in the Sichuan Basin of China. Geofluids 2019 (11), 1–16. https://doi.org/10.1155/2019/8671973.
Han, L.F., Plummer, L.N., Aggarwal, P., 2014. The curved ^{14}C vs. $\delta^{13}C$ relationship in dissolved inorganic carbon: a useful tool for groundwater age-and geochemical interpretations. Chem. Geol. 387, 111–125. https://doi.org/10.1016/j.chemgeo.2014.08.026.
Huang, T., Pang, Z., Li, J., Xiang, Y., Zhao, Z., 2017a. Mapping groundwater renewability using age data in the Baiyang alluvial fan, NW China. Hydrogeol. J. 25 (3), 743–755. https://doi.org/10.1007/s10040-017-1534-z.
Huang, T., Pang, Z., Liu, J.L., Ma, J.Z., Gates, J., 2017b. Groundwater recharge mechanism in an integrated tableland of the Loess Plateau, northern China: insights from environmental tracers. Hydrogeol. J. 25 (7), 2049–2065. https://doi.org/10.1007/s10040-017-1599-8.
Jacobson, A.D., Zhang, Z.F., Lundstrom, C., Huang, F., 2010. Behavior of Mg isotopes during dedolomitization in the Madison Aquifer, South Dakota. Earth. Planet. Sci. Lett. 297 (3–4), 446–452. https://doi.org/10.1016/j.epsl.2010.06.038.
Jiang, G., Hu, S., Shi, Y., Zhang, C., Wang, Z., Hu, D., 2019. Terrestrial heat flow of continental China: updated dataset and tectonic implications. Tectonophysics 753, 36–48. https://doi.org/10.1016/j.tecto.2019.01.006.
Jiang, X., Wan, L., Ge, S., Cao, G., Hou, G., Hu, F., Wang, X., Li, H., Liang, S., 2012. A quantitative study on accumulation of age mass around stagnation points in nested flow systems. Water Resour. Res. 48, W12502. https://doi.org/10.1029/2012wr012509.
Jin, L., Siegel, D.I., Lautz, L.K., Mitchell, M.J., Dahms, D.E., Mayer, B., 2010. Calcite precipitation driven by the common ion effect during groundwater-surface-water mixing: a potentially common process in streams with geologic settings containing gypsum. Geol. Soc. Am. Bull. 122 (7–8), 1027–1038. https://doi.org/10.1130/B30011.1.
Jin, L., Ogrinc, N., Yesavage, T., Hasenmueller, E.A., Ma, L., Sullivan, P.L., Kaye, J., Duffy, C., Brantley, S.L., 2014. The CO_2 consumption potential during gray shale weathering: insights from the evolution of carbon isotopes in the Susquehanna Shale Hills critical zone observatory. Geochim. Cosmochim. Acta 142, 260–280. https://doi.org/10.1016/j.gca.2014.07.006.
Kalacheva, E.G., Taran, Y.A., Voloshina, E.V., Kotenko, T.A., 2018. Geochemistry of thermal waters of Ketoi Island, Kuril Island Arc. J. Volcanol. Seismol. 12 (3), 172–186. https://doi.org/10.1134/S074204631803003x.
Kattan, Z., 2002. Effects of sulphate reduction and geogenic CO_2 incorporation on the determination of ^{14}C groundwater ages – a case study of the Palaeogene groundwater system in north-eastern Syria. Hydrogeol. J. 10 (4), 495–508. https://doi.org/10.1007/s10040-002-0199-3.
Kavouridis, T., Kuris, D., Leonis, C., Liberopoulou, V., Leontiadis, J., Panichi, C., La Ruffa, G., Caprai, A., 1999. Isotope and chemical studies for a geothermal assessment of the island of Nisyros (Greece). Geothermics 28 (2), 219–239. https://doi.org/10.1016/S0375-6505(99)00005-X.
Klimchouk, A.B., 2000. Dissolution and conversions of gypsum and anhydrite. In: Klimchouk, A.B., Ford, D.C., Palmer, A.N., Dreybrodt, W. (Eds.), Speleogenesis: Evolution of Karst Aquifers. Natlional Speleological Society, Huntsville, Alabama.
Kong, Y., Pang, Z., Shao, H., Hu, S., Kolditz, O., 2014. Recent studies on hydrothermal systems in China: a review. Geotherm. Energy 2 (1), 2–19. https://doi.org/10.1186/s40517-014-0019-8.
Kulongoski, J.T., Hilton, D.R., Cresswell, R.G., Hostetter, S., Jacobson, G., 2008. Helium-4 characteristics of groundwaters from Central Australia: comparative chronology with chlorine-36 and carbon-14 dating techniques. J. Hydrol. 348 (1–2), 176–194. https://doi.org/10.1016/j.jhydrol.2007.09.048.
Levet, S., Berger, G., Munoz, M., Toutain, J.P., 2006. A new and fast method to determine mixing and conductive cooling of thermal waters in carbonate-evaporite environments. Geothermics 35 (3), 285–301. https://doi.org/10.1016/j.geothermics.2006.03.002.
Li, T., Li, H., Shen, C., Yang, C., Li, J., Yi, C., Yuan, D., Wang, J., Xie, S., 2010. Study on the δD and $\delta^{18}O$ characeristics of meteoric precipitation during 2006–2008 in Chongqing. Adv. Water Sci. 21 (6), 757–764 (in Chinese).
Lloyd, R.M., 1968. Oxygen isotope behavior in the sulfate-water system. J. Geophys. Res. 73 (18), 6099–6110. https://doi.org/10.1029/JB073i018p06099.
Lu, L., Pang, Z., Kong, Y., Guo, Q., Wang, Y., Xu, C., Gu, W., Zhou, L., Yu, D., 2018. Geochemical and isotopic evidence on the recharge and circulation of geothermal water in the Tangshan Geothermal System near Nanjing, China: implications for sustainable development. Hydrogeol. J. 26 (5), 1705–1719. https://doi.org/10.1007/s10040-018-1721-6.
Ma, R., Wang, Y., Sun, Z., Zheng, C., Ma, T., Prommer, H., 2011. Geochemical evolution of groundwater in carbonate aquifers in Taiyuan, northern China. Appl. Geochem. 26 (5), 884–897. https://doi.org/10.1016/j.apgeochem.2011.02.008.
Mádl-Szőnyi, J., Tóth, Á., 2015. Basin-scale conceptual groundwater flow model for an unconfined and confined thick carbonate region. Hydrogeol. J. 23 (7), 1359–1380. https://doi.org/10.1007/s10040-015-1274-x.
Mao, X., Wang, H., Feng, L., 2018. Impact of additional dead carbon on the circulation estimation of thermal springs exposed from deep-seated faults in the Dongguan basin, southern China. J. Volcanol. Geoth. Res 361, 1–11. https://doi.org/10.1016/j.jvolgeores.2018.08.002.
Marques, J.M., Graca, H., Eggenkamp, H.G.M., Neves, O., Carreira, P.M., Matias, M.J., Mayer, B., Nunes, D., Trancoso, V.N., 2013. Isotopic and hydrochemical data as indicators of recharge areas, flow paths and water-rock interaction in the Caldas da Rainha-Quinta das Janelas thermomineral carbonate rock aquifer (Central Portugal). J. Hydrol. 476, 302–313. https://doi.org/10.1016/j.jhydrol.2012.10.047.
Mayer, B., Krouse, H.R., 2004. Procedures for sulphur isotope abundance studies. Amsterdam, Netherlands In: de Groot, P. (Ed.), Handbook of Stable Isotope Analytical Techniques, pp. 538–596. https://doi.org/10.1016/B978-044451114-0/50028-4.
McMillan, N., Larson, P., Fairley, J., Mulvaney-Norris, J., Lindsey, C., 2018. Direct measurement of advective heat flux from several Yellowstone hot springs, Wyoming, USA. Geosphere 14 (4), 1860–1874. https://doi.org/10.1130/Ges01598.1.
Meredith, K.T., Han, L.F., Hollins, S.E., Cendón, D.I., Jacobsen, G.E., Baker, A., 2016. Evolution of chemical and isotopic composition of inorganic carbon in a complex semi-arid zone environment: consequences for groundwater dating using radiocarbon. Geochim. Cosmochim. Acta 188, 352–367. https://doi.org/10.1016/j.gca.2016.06.011.
Mook, W.G., 2000. Environmental Isotopes in the Hydrological Cycle: Principles and Applications. UNESCO, Paris.
Pang, Z.H., 2001. Isotope and chemical geothermometry and its applications. Sci. China Ser. E 44, 16–20. https://doi.org/10.1007/Bf02916784.
Pang, L., Chen, S., Huang, W., Wu, Y., Wei, G., 2017. Paleoenvironmental and chronological analysis of the mammalian fauna from Migong Cave in the Three Gorges

Area. China. Quatern. Int. 434, 25–31. https://doi.org/10.1016/j.quaint.2014.11.039.
Pang, Z.H., Reed, M., 1998. Theoretical chemical thermometry on geothermal waters: problems and methods. Geochim. Cosmochim. Acta 62 (6), 1083–1091. https://doi.org/10.1016/S0016-7037(98)00037-4.
Pang, Z.H., Hu, S.B., Wang, J.Y., 2012. A roadmap to geothermal energy development in China. Sci. Technol. Rev. 30 (32), 18–24 (in Chinese).
Pang, Z.H., Kong, Y.L., Shao, H.B., Kolditz, O., 2018. Progress and perspectives of geothermal energy studies in China: from shallow to deep systems. Environ. Earth Sci. 77 (16). https://doi.org/10.1007/s12665-018-7757-z.
Parkhurst, D.L., Appelo, C.A.J., 2013. Description of Input and Examples for PHREEQC Version 3—A Computer Program for Speciation, Batch-Reaction, One-Dimensional Transport, and Inverse Geochemical Calculations. U.S. Geological Survey Techniques and Methods, book 6, chap. A43, 497p. Available only at http://pubs.usgs.gov/tm/06/a43/.
Piper, M., 1944. A graphic procedure in the geochemical interpretation of water-analyses. Trans. Am. Geophys. Union 25 (6), 914–928. https://doi.org/10.1029/TR025i006p00914.
Pu, J., Yuan, D., Zhang, C., Zhao, H., 2013. Hydrogeochemistry and possible sulfate sources in karst groundwater in Chongqing, China. Environ. Earth Sci. 68 (1), 159–168. https://doi.org/10.1007/s12665-012-1726-8.
Qiu, X., Wang, Y., Wang, Z., Regenauer-Lieb, K., Zhang, K., Liu, J., 2018. Determining the origin, circulation path and residence time of geothermal groundwater using multiple isotopic techniques in the Heyuan Fault Zone of Southern China. J. Hydrol. 567, 339–350. https://doi.org/10.1016/j.jhydrol.2018.10.010.
Raines, M.A., Dewers, T.A., 1997. Dedolomitization as a driving mechanism for karst generation in Permian Blaine formation, southwestern Oklahoma, USA. Carbonate. Evaporite 12 (1), 24–31. https://doi.org/10.1007/Bf03175799.
Renac, C., Gal, F., Menot, R.P., Squarcioni, P., Perrache, C., 2009. Mean recharge times and chemical modelling transfers from shallow groundwater to mineralized thermal waters at Montrond-les-Bains, Eastern Massif Central, France. J. Hydrol. 376 (1–2), 1–15. https://doi.org/10.1016/j.jhydrol.2009.07.011.
Shestakova, A.V., Guseva, N.V., 2018. Calculation of deep temperatures of thermal waters in Eastern Tuva. Bull. Tomsk Polytech. Univ.-Geo Assets Eng. 329 (1), 25–36.
Stober, I., Zhong, J., Zhang, L., Bucher, K., 2016. Deep hydrothermal fluid-rock interaction: the thermal springs of Da Qaidam, China. Geofluids 16 (4), 711–728. https://doi.org/10.1111/gfl.12190.
Strauss, H., 1997. The isotopic composition of sedimentary sulfur through time. Palaeogeogr. Palaeocl. 132 (1–4), 97–118. https://doi.org/10.1016/S0031-0182(97)00067-9.
Stute, M., Deak, J., 1989. Environmental isotope study (^{14}C, ^{13}C, ^{18}O, D, Noble Gases) on deep groundwater circulation systems in Hungary with reference to paleoclimate. Radiocarbon 31 (3), 902–918. https://doi.org/10.1017/S0033822200012522.
Szijártó, M., Galsa, A., Tóth, Á., Mádl-Szőnyi, J., 2019. Numerical investigation of the combined effect of forced and free thermal convection in synthetic groundwater basins. J. Hydrol. 572, 364–379. https://doi.org/10.1016/j.jhydrol.2019.03.003.
Ta, M., Zhou, X., Guo, J., Wang, Y., Wang, X., Xu, Y., 2019. Hydrogeochemical characteristics and formation of the hot springs occurring in the plunging ends of an anticline in Chongqing, Eastern Sichuan Basin, China. Environ. Earth Sci. 78, 486. https://doi.org/10.1007/s12665-019-8486-7.
Tamers, M.A., 1975. Validity of radiocarbon dates on groundwater. Surv. Geophys. 2, 217–239. https://doi.org/10.1007/BF01447909.
Tian, J., Pang, Z., Guo, Q., Wang, Y., Li, J., Huang, T., Kong, Y., 2018. Geochemistry of geothermal fluids with implications on the sources of water and heat recharge to the Rekeng high-temperature geothermal system in the Eastern Himalayan Syntax. Geothermics 74, 92–105. https://doi.org/10.1016/j.geothermics.2018.02.006.
Tole, M.P., Ármannsson, H., Pang, Z., Arnórsson, S., 1993. Fluid/mineral equilibrium calculations for geothermal fluids and chemical geothermometry. Geothermics 22 (1), 17–37. https://doi.org/10.1016/0375-6505(93)90018-I.
Tóth, J., 1963. A theoretical analysis of groundwater flow in small drainage basins. J. Geophys. Res. 68 (16), 4795–4812. https://doi.org/10.1029/Jz068i008p02354.
Tóth, J., 1995. Hydraulic continuity in large sedimentary basins. Hydrogeol. J. 3 (4), 4–16. https://doi.org/10.1007/s100400050250.
Utting, N., Lauriol, B., Mochnacz, N., Aeschbach-Hertig, W., Clark, I., 2013. Noble gas and isotope geochemistry in western Canadian Arctic watersheds: tracing groundwater recharge in permafrost terrain. Hydrogeol. J. 21 (1), 79–91. https://doi.org/10.1007/s10040-012-0913-8.
Verma, S.P., Santoyo, E., 1997. New improved equations for Na/K, Na/Li and SiO_2 geothermometers by outlier detection and rejection. J. Volcanol. Geoth. Res 79, 9–23. https://doi.org/10.1016/S0377-0273(97)00024-3.
Vogel, J.C., 1993. 4 – variability of carbon isotope fractionation during photosynthesis. In: Ehleringer, J.R., Hall, A.E., Farquhar, G.D. (Eds.), Stable Isotopes and Plant Carbon-water Relations. Academic Press, San Diego, pp. 29–46. https://doi.org/10.1016/B978-0-08-091801-3.50010-6.
Wang, P., Chen, X., Shen, L., Wu, K., Huang, M., Xiao, Q., 2016. Geochemical features of the geothermal fluids from the Mapamyum non-volcanic geothermal system (Western Tibet, China). J. Volcanol. Geotherm. Res. 320, 29–39. https://doi.org/10.1016/j.jvolgeores.2016.04.002.
Wang, G., Li, K., Wen, D., Lin, W., Lin, L., Liu, Z., Zhang, W., Ma, F., Wang, W., 2013. Assessment of Geothermal Resources in China, Thirty-Eighth Workshop on Geothermal Reservoir Engineering. Stanford University, Stanford, California.
Xiao, Q., Jiang, Y., Shen, L., Yuan, D., 2018. Origin of calcium sulfate-type water in the Triassic carbonate thermal water system in Chongqing, China: a chemical and isotopic reconnaissance. Appl. Geochem. 89, 49–58. https://doi.org/10.1016/j.apgeochem.2017.11.011.
Yang, P., Cheng, Q., Xie, S., Wang, J., Chang, L., Yu, Q., Zhan, Z., Chen, F., 2017. Hydrogeochemistry and geothermometry of deep thermal water in the carbonate formation in the main urban area of Chongqing, China. J. Hydrol. 549, 50–61. https://doi.org/10.1016/j.jhydrol.2017.03.054.
Yang, P., Dan, L., Groves, C., Xie, S., 2019. Geochemisitry and genesis of geohtermal well water from a carbonate-evaporite aquifer in Chongqing, SW China. Environ. Earth Sci. 78, 33. https://doi.org/10.1007/s12665-018-8004-3.
Yang, F., Pang, Z., Lin, L., Jia, Z., Zhang, F., Duan, Z., Zong, Z., 2013. Hydrogeochemical and isotopic evidence for trans-formational flow in a sedimentary basin: Implications for CO_2 storage. Appl. Geochem. 30, 4–15. https://doi.org/10.1016/j.apgeochem.2012.08.024.